Magnetic Hysteresis Effects in Superconducting Titanium Nitride Microwave Resonators

Diplomarbeit

von

Philipp Mayer

6. Juni 2013

Referent: **Prof. Dr. A.V. Ustinov**
Korreferent: Prof. Dr. G. Weiß

Contents

Zusammenfassung

Elektrische Resonatoren finden in zahlreichen Bereichen Anwendung, weshalb es nicht weiter verwunderlich erscheint, dass sie auch in supraleitenden Schaltkreisen verwendet werden. Obwohl supraleitende Resonatoren schon seit den 1960er Jahren untersucht wurden, ist vor allem in jüngster Zeit das Interesse an ihnen extrem gestiegen. Sie werden hauptsächlich als Mikrowellendetektoren für kosmische Hintergrundstrahlung und als Bestandteile supraleitender Schaltkreise verwendet. Ein wesentlicher Vorteil supraleitender Resonatoren liegt in ihrem hohen Signal-zu-Rausch-Verhältnis und geringen energetischen Verlusten. In Schaltkreisen werden supraleitende Resonatoren als Ausleseelemente von Qubits verwendet. Man kann sie aber auch als Speicherelemente oder Bussysteme einsetzen um verschiedene Qubits miteinander zu koppeln. Da in jüngster Zeit große Fortschritte auf dem Gebiet der supraleitenden Qubits erzielt wurden, vor allem durch höhere Kohärenzzeiten, ist auch das Interesse an supraleitenden Resonatoren stark gewachsen. Hierbei liegt das Augenmerk hauptsächlich auf der Erhöhung der Gütefaktoren. Diese sind durch verschiedene Verlustmechanismen, wie Quasiteilchen und Zweiniveausysteme limitiert.

Doch supraleitende Resonatoren finden nicht nur in Schaltkreisen Anwendung, es ist auch möglich sie an andere Quantensysteme zu koppeln. Hierfür kommen verschiedene Systeme in Frage, zum Beispiel Moleküle, Elektronen, Elektronenspin-Ensembles in Kristallen oder Wolken ultrakalter Atome. Da solche Systeme Magnetfelder zur Kontrolle oder Lokalisierung benötigen, wird der Resonator zwangsläufig ebenfalls im Magnetfeld betrieben. Aufgrund dessen ist es wichtig das Verhalten supraleitender Resonatoren im Magnetfeld zu verstehen.

Resonatoren werden maßgeblich durch ihren Gütefaktor und ihre Resonanzfrequenz beschrieben. Beide erfahren eine Reduktion wenn sie im Magnetfeld betrieben werden, wobei sich auch Hystereseeffekte zeigen. Eine Erkärung für die zusätzlichen Verluste wurde von Bothner *et al.* gegeben [1], bei der angenommen wird, dass die Vortizes oszillieren und somit Energie dissipiert wird. Berücksichtigt man in diesem Modell die inhomogene Strom-und Vortexverteilung, so lassen sich auch Hystereseeffekte erklären.

Diese Arbeit beschäftigt sich mit sogenannten Typ 2 Supraleitern, welche das Eintreten von Vortizes oberhalb eines kritischen Magnetfeldes H_{c1} erlauben. Das Ziel ist hierbei das magnetische Verhalten supraleitender Resonatoren besser zu verstehen. Ein Fokus liegt dabei auf den magnetischen Hystereseeffekten der Resonanfrequenz und des Gütefaktors.

Ein Teil dieser Diplomarbeit bestand darin, einen Prozess zur Strukturierung von supraleitenden Resonatoren zu etablieren. Als Material wurde Titannitrid verwendet, das vielversprechende Eigenschaften aufweist. Als Substrat wählten wir intrinsisches Silizium. Titannitrid ist mechanisch sehr stabil und chemisch inert. Die Sprungtemperatur T_c hängt von der Zusammensetzung ab und erreicht Werte bis zu fünf Kelvin. Dies hat zur Folge, dass für die Untersuchung solcher Resonatoren Temperaturen unterhalb der Siedetemperatur von Helium bei Atmosphärendruck erforderlich sind. Desweiteren wurden für TiN-Resonatoren in der Vergangenheit bereits hohe Gütefaktoren erzielt. Ein weiterer Vorteil ist, dass Titannitrid eine hohe kinetische Induktivität aufweist. Dies ist für unsere Zwecke von Vorteil, da die kinetische Induktivität die Frequenzverschiebung im Magnetfeld verursacht.

Die in dieser Arbeit verwendeten Resonatoren wurden komplett im CFN Reinraum des KIT mittels Photolithographie strukturiert. Die Resonatorfelder wurden zunächst am PC designt und analysiert. Es wurden Resonatoren unterschiedlicher Geometrien erstellt, wie $\frac{\lambda}{2}$- und $\frac{\lambda}{4}$-Resonatoren sowie LC-Schwingkreise. Danach wurde mittels Laserlithographie eine Fotomaske mit verschiedenen Resonatorfeldern erstellt. Anschließend wurde auf die Chips Fotolack aufgeschleudert. Als nächstes wurden die erwünschten Bereiche mithilfe der Fotomaske und eines Maskaligners belichtet. Nach Entwicklung des Fotolacks wurde das Titannitrid in den frei liegenden Gebieten mittels Plasmaätzen entfernt. Als Ätzgas wurde hierfür Schwefelhexafluorid verwendet. Es weist beim Ätzen eine hohe Selektivität auf und entfernt Silizium zwanzig mal schneller als Titannitrid. Dies führt zu tiefen Einschnitten im Substrat, was sich positiv auf den Gütefaktor auswirkt.

Für unsere Messungen verwendeten wir einen Chip mit 14 $\frac{\lambda}{4}$-Resonatoren mit kalkulierten Resonanzfrequenzen zwischen 4 und 10 GHz. Diese Resonatoren wurden mittels eines sogenannten Helium 3 Dipsticks analysiert. Durch Verwendung des Isotops He3 und Verringerung des Dampfdrucks können Temperaturen bis zu 300 Millikelvin erreicht werden. Wir führten Transmissionsmessungen mit einem Netzwerkanalysator durch, wobei die Resonatoren sich als lorentzförmige Vertiefungen bemerkbar machten. Die benötigten Parameter wurden mithilfe eines gefitteten Kreises in der komplexen Ebene bestimmt.

Zunächst bestimmten wir Gütefaktoren, Resonanzfrequenzen und Kopplungsstärken der einzelnen Resonatoren, wobei wir für die Resonanzfrequenzen eine geringe Verschiebung aufgrund der kinetischen Induktivität feststellen. Der größte gemessene Gütefaktor beträgt 190 000. Wir ermittelten Hysteresekurven für Resonatoren unterschiedlicher Frequenz bei Temperaturen von 300 mK. Hierfür wurde das Magnetfeld schrittweise erhöht und anschließend wieder reduziert, wobei nach jedem Schritt die Resonatorparameter ermittelt wurden. Sowohl die Änderungen in Resonanzfrequenz als auch im Gütefaktor zeigten eine Hysteresekurve. Die relative Änderung der Resonanzfrequenz war unabhängig von den untersuchten Resonatoren stets die gleiche. Ursache hierfür ist eine Änderung der kinetischen Induktivität, die antiproportional zur Resonanzfrequenz ist. Auch die Verluste wiesen deutliche Hystereseeffekte auf, wobei diese bei verschiedenen Resonatoren unterschiedlich stark ausgeprägt waren.

Wir untersuchten auch die Temperaturabhängigkeit eines Resonators im Bereich zwischen 300

mK und 900 mK, wobei wir eine starke Temperaturabhängigkeit, vor allem des Gütefaktors, feststellten. Dieser verringerte sich bei Erhöhen der Temperatur auf ein Kelvin auf ein Fünftel des ursprünglichen Werts. Desweiteren untersuchten wir den Einfluss der eingehenden Leistung, konnten hier aber über einen Bereich von 25 dB nur geringe Änderungen feststellen.

Abschließend lässt sich Zusammenfassen, dass supraleitende Resonatoren nur im Magnetfeld betrieben werden sollten, wenn es sich nicht vermeiden lässt. Falls es doch notwendig ist, so lassen sich die unerwünschten verluste minimieren. Dies kann zum einen durch eine Anpassung der Resonatorstruktur erreicht werden. Es ist jedoch ebenfalls möglich dies durch entsprechende Anpassung der magnetischen Vorgeschichte zu erreichen.

Contents

Introduction and Motivation

Superconducting resonators have been studied since the 1960s. Over the last few years they have become a very active research field. Superconducting resonators are used as microwave detectors and for superconducting circuit quantum electrodynamics because of their low signal-to-noise ratio and low dissipation. The increasing interest has been caused by the demonstration of transmission line resonators as photon detectors [2] and the adoption of these resonators as a quantum state readout of superconducting qubits. In circuit quantum electrodynamics, superconducting resonators are also used as a quantum bus or a memory storing the information of a qubit. It is also possible to couple them to other quantum systems like trapped magnetic molecules, electrons, electron spins in a crystal or ultracold atomic clouds [3, 4, 5, 6, 7]. Since such quantum systems require magnetic fields, the resonators are operated in them. Therefore the magnetic behaviour of resonators is of great interest. In the past changes in frequency and quality factor depending on the applied magnetic field and magnetic field history have been observed [8, 9, 1]. There have also been achievements to reduce these changes by implementing flux traps in the resonator structure [10, 11, 12].
Using optical lithography, we structured resonators made out of titanium nitride. This material is very promising because quality factors of more than one million at single photon levels have been demonstrated [13]. Resonators of this material feature a large kinetic inductance. We investigate the behaviour of quarter wavelength resonators in a perpendicular magnetic field. The influence of the magnetic field history is analysed as well. The measurements were done in a helium 3 setup which reaches temperatures down to 300 mK. All the required parameters were determined with a circle fit considering both quadratures.

In the first chapter of this thesis a theoretical overview of the basics of superconductivity is given. The magnetic behaviour of type 2 superconductors is discussed in the second chapter. At first the Bean model for hard superconductors is introduced [14], which describes the vortex distribution in superconductors. Afterwards the Norris-Brandt-Indenbom model is presented [15, 16], a model that enhances the one given by Charles P. Bean. Furthermore a mechanism for changes and magnetic hysteresis effects in resonance frequency and quality factor is given. The third chapter deals with the patterning process, which was done at the CFN cleanroom. The fourth chapter focuses on the measurement setup and the fitting procedure. Finally, the last chapter highlights and discusses our measurements.

Contents

Chapter 1

Theory

1.1 Superconductivity

In 1911 Heike Kamerlingh Onnes discovered the vanishing of the electrical resistance of mercury using a technique to liquify Helium [17]. This phenomenon occurred for other materials below the material specific critical temperature T_c in further experiments. In 1933 Walther Meissner and Robert Ochsenfeld found out that superconductors below the critical temperature expel a magnetic field completely [18]. This so-called Meissner effect was observed whether the sample was cooled down after applying a magnetic field or vice versa. This behaviour indicates that superconductivity is a thermodynamical state. Further experiments showed that the superconducting state could not only be destroyed by heating the sample above T_c, but also by exceeding a critical magnetic field H_c. This critical magnetic field shows a temperature dependence [19]:

$$H_c \approx H_c(T = 0) \left(1 - \left(\frac{T}{T_c} \right)^2 \right) \tag{1.1}$$

F. and H. London were able to explain the principal behaviour of a superconductor by introducing two equations [20]:

$$\vec{E} = \frac{\partial}{\partial t}(\Lambda_L \vec{J}_s) \tag{1.2}$$

$$\vec{\nabla} \times (\Lambda_L \vec{J}_s) = -\frac{1}{c}\vec{H} \tag{1.3}$$

$$\Lambda = \frac{4\pi\lambda_L^2}{c^2} = \frac{m_e}{n_s e^2} \tag{1.4}$$

$\vec{J}_s$ denotes the superconducting current, λ_L the London penetration depth, n_s the density of the superconducting electrons, c the light velocity in vacuum, m_e the electron mass and e its charge. The first equation replaces Ohm's law, describing lossless conductivity. According to this equation an electric field accelerates the electrons instead of maintaining their velocity. Combining the second equation with the Maxwell equation $\nabla \times \vec{H} = 4\pi\vec{J}/c$ leads to

$$\nabla^2 \vec{H} = \frac{\vec{H}}{\lambda_L^2} \tag{1.5}$$

This explains the Meissner effect with a magnetic field exponentially screened from the interior of the superconductor. In 1950 Ginzburg and Landau presented a theory that was able to explain some effects that had not been understood before [21]. In their theory, a complex pseudowavefunction ψ was introduced, which is an order parameter in the theory of second order phase transitions. Another parameter employed there is the coherence length η:

$$\eta(T) = \frac{\hbar}{\sqrt{|2m\alpha(T)|}} \tag{1.6}$$

Here $\alpha(T)$ is an expansion coefficient of the free energy and $\hbar$ is the reduced planck constant. The coherence length characterises the distance over which ψ can vary with only little change in energy. The ratio of penetration depth and coherence length is the GL parameter κ, which characterises the magnetic behaviour of the superconductor:

$$\kappa = \frac{\lambda_L}{\eta} \tag{1.7}$$

The next step in understanding superconductivity was the BCS theory, named after their authors Bardeen, Cooper and Schrieffer. It explains superconductivity with an interaction between two electrons. They form a so-called Cooper pair with an integer spin. Cooper pairs can be treated as bosons and thus all adopt the same quantum mechanical state. This state can be described by a single macroscopical wavefunction. A minimal energy of 2Δ is required to break a Cooper pair. Δ is the so-called energy gap.

1.1.1 Two Fluid Model

The main assumption of this model [22] is that all free electrons of a superconductor can be separated into two groups. One group contains all the superconducting electrons of density n_s and the other group all the normal electrons of density n_n. At zero temperature all the electrons are superconducting ones.
However, electrons get thermally excited as the temperature increases. As a consequence, they become normal conducting. The temperature dependence of the superconducting electrons is given by:

$$\frac{n_s}{n} = 1 - \left(\frac{T}{T_c}\right)^4 \tag{1.8}$$

Uncoupled electrons are considered as elementary excitations of the superconductor and are also called quasiparticles.

1.1.2 Type 2 Superconductors

Apart from superconductors that show the described behaviour, there exists another type. These so-called type 2 or hard superconductors differ in their magnetic behaviour. They expel magnetic fields completely up to a lower critical field H_{c1}. If the magnetic field exceeds this
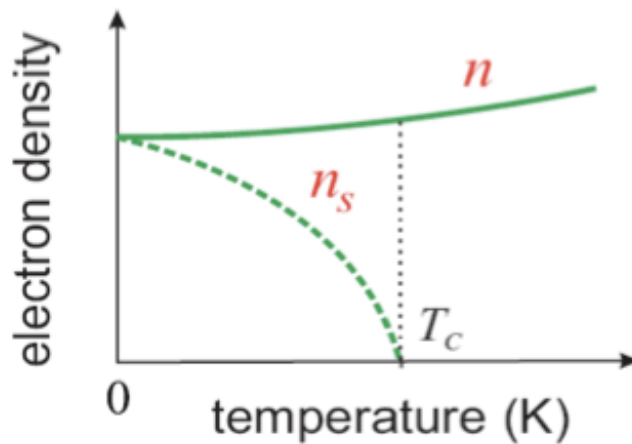
Fig. 1.1: Temperature dependence of electron density and superconducting electron density [23].

value, it starts to penetrate the superconductor in the form of so-called Abrikosov vortices. Each vortex carries a magnetic flux quantum $\Phi_0 = \frac{h}{2e}$. A circular current flows around each vortex, which arouses a repulsive force between them. The vortices arrange themselves in a triangular lattice. When the magnetic field is increased further, more vortices enter the superconductor and the distance between them decreases. The phase between zero-field and H_{c1} is called Meissner phase and the phase between H_{c1} and H_{c2} Shubnikov phase. If the magnetic field exceeds the value H_{c2}, superconductivity vanishes completely.

The magnetic behaviour of a superconductor is determined by κ. If κ is smaller than $\frac{1}{\sqrt{2}}$ it behaves as a type 1 superconductor. For bigger values the superconductor is of type 2. Most elemental superconductors are type 1 superconductors, like mercury or lead. Examples for type 2 superconductors are niobium and all high temperature superconductors.

1.2 Microwave Resonators

In our work we focus on two types of superconducting resonators: lumped element and coplanar waveguide (CPW) resonators. Lumped element resonators comprise a capacitor and an inductor either in a parallel or a series geometry. CPW resonators simply consist of a stripline between two groundplanes. The energy stored in a resonator is determined by its resonance frequency f_0 and the number of the stored photons n.

$$E = nhf_0 \tag{1.9}$$

1.2.1 Quality Factor

A resonator is basically described by two characteristics: Its resonance frequency and its quality factor. The quality factor describes how long the stored energy remains in the resonator. It is

defined as

$$Q = 2\pi \frac{\text{stored energy}}{\text{energy lost per cycle}} \tag{1.10}$$

There is a difference between the total and the internal quality factor. The internal quality factor Q_i is an intrinsic characteristic of the resonator. The total or loaded quality factor Q_L also depends on other properties, like the coupling to the environment and the feedline. The quality factors are related by:

$$\frac{1}{Q_L} = \frac{1}{Q_i} + \frac{1}{Q_c} \tag{1.11}$$

Q_c is the coupling quality factor. The coupling quality factors describes how strong the resonator is coupled to the feedline.

Another way to describe the losses of a resonator is given by the loss tangent. It is defined as the ratio of the real and the imaginary part of the impedance:

$$\tan(\delta) = \frac{R}{X} \tag{1.12}$$

It is related to the quality factor by:

$$\tan(\delta) = \frac{1}{Q_i} \tag{1.13}$$

In superconducting resonators δ is usually very small (in the range of 10^{-3} to 10^{-7}) so this formula can be approximated by:

$$\delta = \frac{1}{Q_i} \tag{1.14}$$

There are different mechanisms that reduce the quality factor. An advantage of describing these mechanisms via the losses is that the total loss can be derived easily by adding up all loss components.

1.2.2 Lumped Element Resonators

These resonators are formed of a capacitor and an inductor. Lumped element means that the size of the components is small compared to the photon wavelength, which is typically some millimeters. The inductor is often realised by a meandered stripline. The capacitor is usually formed by finger structures that gear into each other. In every resonator energy is exchanged periodically between the capacitor and the inductor.

The resonance frequency of an LC circuit is given by:

$$f_0 = \frac{1}{2\pi\sqrt{LC}} \tag{1.15}$$

The angular frequency is

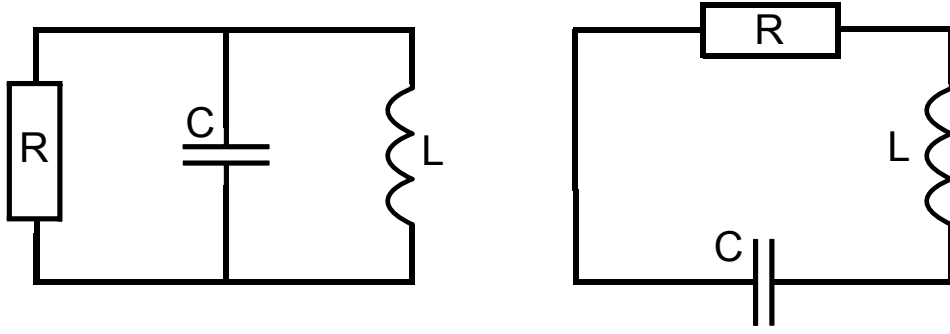$$\omega_0 = 2\pi f_0 = \frac{1}{\sqrt{LC}} \tag{1.16}$$

Fig. 1.2: Scheme of a parallel (left) and a series RLC circuit (right)

Although we use a superconductor, there are still dissipation mechanisms such as losses due to quasiparticles or two level systems. These mechanisms are taken into account by adding a resistor of resistance R to our system. Since current and voltage are oscillating, the system is characterised by its impedance $Z = \frac{U(t)}{I(t)}$. This impedance can be split into a real and an imaginary part

$$Z_{in} = R + iX \tag{1.17}$$

with the resistance R and the reactance X. At the resonance frequency the reactance becomes zero. The following section provides an overview of some resonator properties on the basis of the book Microwave engineering of D. M. Pozar [24].

Series Resonant Circuit

The average magnetic energy stored in the inductor is

$$W_m = \frac{1}{4}L|I_{max}|^2 \tag{1.18}$$

$$W_e = \frac{1}{4}C|V_{max}|^2 = \frac{|I_{max}|^2}{4\omega^2 C} \tag{1.19}$$

calculates the average electrical energy stored in the capacitor.
Dissipation takes place at the resistor. The dissipated power is

$$P = \frac{1}{2}|I_{max}|V_{max} = \frac{1}{2}|I_{max}|^2 R \tag{1.20}$$

The input impedance for a series RLC circuit satisfies the following equation:

$$Z_{in} = R + iX = R + i\left(\omega L - \frac{1}{\omega C}\right) \tag{1.21}$$

According to Kirchhoff the current in every element is the same, so the input power can be derived by:

$$P_{in} = \frac{1}{2}Z_{in}|I_{max}|^2 = \frac{1}{2}|I_{max}|^2\left(R + i\left(\omega L - \frac{1}{\omega C}\right)\right) \tag{1.22}$$

The input impedance can be expressed as:

$$Z_{in} = \frac{2P_{in}}{|I_{max}|^2} = \frac{P_{loss} + 2i\omega(W_m - W_e)}{\frac{1}{2}|I_{max}|^2} \tag{1.23}$$

At resonance frequency the average energy stored in the inductor W_m is the same as the energy in the capacitor W_e and the imaginary part of Z_{in} vanishes. This leads to:

$$\omega_0 = \frac{1}{\sqrt{LC}} \tag{1.24}$$

The quality factor for a series RLC circuit is given by:

$$Q_i = \frac{1}{\omega RC} \tag{1.25}$$
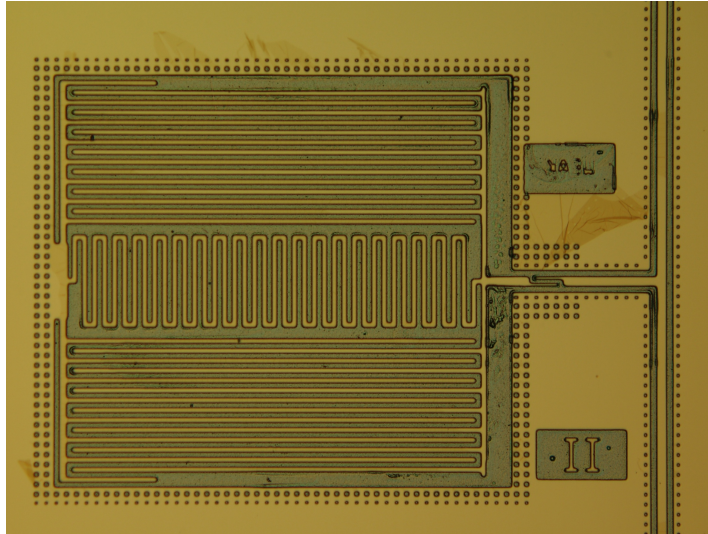
Parallel Resonant Circuit

Fig. 1.3: Parallel lumped LC resonator with finger capacitors illustrated at the top and bottom. The meandered inductor is shown in the middle. The resonator is coupled capacitively to a feedline on the right. The brighter regions are the superconductor and the small dark dots are flux traps. The resonator was fabricated during this work.

The average energy stored in the inductor and the capacitor of a parallel resonant circuit is given by the following equations:

$$W_m = \frac{1}{4}L|I_{max}|^2 = \frac{|V_{max}^2|}{4\omega^2 L} \tag{1.26}$$

$$W_e = \frac{1}{4}C|V_{max}|^2 \tag{1.27}$$

The dissipated power at the resistor is

$$P = \frac{|V_{max}|^2}{2R} \tag{1.28}$$

The input impedance of a parallel RLC circuit is calculated by

$$Z_{in} = \left(\frac{1}{R} + \frac{1}{i\omega L} + i\omega C \right)^{-1} \tag{1.29}$$

In a parallel resonant circuit the voltage at every element is the same, hence the input power can be derived by:

$$P = \frac{|V_{max}|^2}{2Z_{in}^*} = \frac{1}{2}|V_{max}|^2 \left(\frac{1}{R} + i \left(\frac{1}{\omega L} - \omega C \right) \right) \tag{1.30}$$

In addition the input impedance can be written as:

$$Z_{in} = \frac{2P_{in}}{|I_{max}|^2} = \frac{P_{loss} + 2i\omega(W_m - W_e)}{\frac{1}{2}|I_{max}|^2} \tag{1.31}$$

The imaginary part of this equation becomes zero if the average energy stored in the capacitor equals the average energy in the inductor. This condition is fulfilled at the resonance frequency, which is:

$$\omega_0 = \frac{1}{\sqrt{LC}} \tag{1.32}$$

For a parallel RLC circuit the quality factor is given by:

$$Q_i = \omega RC \tag{1.33}$$

1.2.3 Coplanar Waveguide Resonators

A coplanar waveguide resonator (CPW) consists of a long strip that may be meandered. It is either shorted to ground ($\frac{\lambda}{4}$-) or open ended ($\frac{\lambda}{2}$-resonator).

Fig. 1.4: $\frac{\lambda}{4}$-resonator coupled inductively to a feedline. The brighter regions are superconductor; the small dots in the ground plane are flux traps. The resonator was fabricated during this work.

The resonance frequency for such a resonator is determined by its length and the light velocity in the material. For $\frac{\lambda}{4}$-resonators the fundamental mode is

$$f_0 = \frac{c}{4l\sqrt{\epsilon_{\text{eff}}}} \tag{1.34}$$

c is the light velocity, l the total length of the strip and ϵ_{eff} denotes the effective dielectric constant, which is the average dielectric constant seen by the superconductor. If the strip width is big compared to the film thickness it can be approximated by:

$$\epsilon_{\text{eff}} = \frac{\epsilon_{\text{substrate}} + 1}{2} \tag{1.35}$$

The higher modes of the resonance frequency are

$$f_n = (2n + 1)f_0, \quad n \in \mathbb{N} \tag{1.36}$$

For $\frac{\lambda}{2}$-resonators the fundamental mode is

$$f_0 = \frac{c}{2l\sqrt{\epsilon_{\text{eff}}}} \tag{1.37}$$

and the higher modes are

$$f_n = (n + 1)f_0, \ n \in \mathbb{N} \tag{1.38}$$

Geometric capacitance and inductance can be calculated by using the conformal Schwarz-Christoffel mapping technique [25]. The film thickness is assumed to be zero. The relevant parameter to derive capacitance and inductance is k, which is the ratio of the distance between the ground planes and the strip width. With this parameter the complete elliptic integrals are:

$$K = K(k) = \int_0^1 \frac{1}{\sqrt{(1 - x^2)(1 - k^2 x^2)}} dx \tag{1.39}$$

$$K' = K(k') = \int_1^{1/k} \frac{1}{\sqrt{(x^2 - 1)(1 - k^2 x^2)}} dx \tag{1.40}$$

where $k' = \sqrt{1 - k^2}$. With this parameters the capacitance per length is:

$$C' = \epsilon_{\text{eff}}\epsilon_0 \frac{4K}{K'} \tag{1.41}$$

And the inductance per length:

$$L' = \mu_0 \frac{K}{4K'} \tag{1.42}$$

The inductance, capacitance and resistance of CPW resonators can be assigned if they are treated as an RLC circuit. The input impedance of a quarter wavelength resonator is:

$$Z_{in} \simeq \frac{Z_0}{\alpha l + i\pi\Delta\omega/2\omega_0} \tag{1.43}$$

α is the attenuation constant and Z_0 the characteristic impedance of the transmission line. The formula is of the same form as the impedance of a parallel RLC circuit, so the formulas can be derived analogously.

$$R = \frac{Z_0}{\alpha l} \tag{1.44}$$

$$C = \frac{\pi}{4\omega_0 Z_0} \tag{1.45}$$

$$L = \frac{1}{\omega_0^2 C} \tag{1.46}$$

The internal quality factor is:

$$Q_i = \omega_0 R C = \frac{\pi}{4\alpha l} \tag{1.47}$$

The input impedance of an open-circuited half wavelength resonator is:

$$Z_{in} \simeq \frac{Z_0}{\alpha l + i\pi(\Delta\omega)/\omega_0} \tag{1.48}$$

The formula is of the same form as the impedance of a parallel RLC circuit. Resistance, capacitance and inductance are:

$$R = \frac{Z_0}{\alpha l} \tag{1.49}$$

$$C = \frac{\pi}{2\omega_0 Z_0} \tag{1.50}$$

$$L = \frac{1}{\omega_0^2 C} \tag{1.51}$$

Then the quality factor can be derived by:

$$Q_i = \omega_0 R C = \frac{\pi}{2\alpha l} \tag{1.52}$$

With these values the resonance frequency can also be written as:

$$f_0 = \frac{1}{2\pi\sqrt{LC}} \tag{1.53}$$

1.2.4 Resonator Response

Microwave circuits are typically characterised by their scattering parameters, which correspond to the ratio of the voltages between the ports. The scattering parameters are defined as:

$$S_{11} = \frac{V_1^-}{V_1^+} \qquad S_{12} = \frac{V_1^-}{V_2^+} \tag{1.54}$$

$$S_{21} = \frac{V_2^-}{V_1^+} \qquad S_{22} = \frac{V_2^-}{V_2^+} \tag{1.55}$$

Here V_n^- denotes the outgoing voltage and V_n^+ the incoming voltage from port n. These parameters can be described for a two port system via the ABCD matrix [24]. The ABCD matrix satisfies the following equation:

$$\begin{pmatrix} V_1 \\ I_1 \end{pmatrix} = \begin{pmatrix} A & B \\ C & D \end{pmatrix} \begin{pmatrix} V_2 \\ I_2 \end{pmatrix} \tag{1.56}$$

The scatter parameters are connected to the parameters of the ABCD matrix by the following equations:

$$S_{11} = \frac{A + B/Z_0 - CZ_0 - D}{A + B/Z_0 + CZ_0 - D} \qquad S_{12} = \frac{2(AD - BC)}{A + B/Z_0 + CZ_0 + D} \tag{1.57}$$

$$S_{21} = \frac{2}{A + B/Z_0 + CZ_0 + D} \qquad S_{22} = \frac{-A + B/Z_0 - CZ_0 - D}{A + B/Z_0 + CZ_0 - D}$$

A $\frac{\lambda}{4}$-resonator has a shunt impedance to ground. It has the following ABCD matrix:

$$\begin{pmatrix} A & B \\ C & D \end{pmatrix} = \begin{pmatrix} 1 & 0 \\ Y & 1 \end{pmatrix} \tag{1.58}$$

With $Y = \frac{1}{Z_{in}}$. In this thesis we only consider the transmission S_{12} or S_{21}. For quarter wavelength resonators they reduce to:

$$S_{12} = S_{21} = \frac{2}{2 + Z_0/Z_{in}} \tag{1.59}$$

Z_0 denotes the characteristic impedance, which is usually 50 Ω for the microwave cables as well as for the transmission line on the chip. Far away from the resonance frequency the impedance Z_{in} becomes very large, leading to almost full transmission. At the resonance frequency, however, transmission is minimal. If the amplitude and phase of S_{21} are plotted separately the real part shows a Lorentz function and the imaginary part an arcus tangens profile.

1.2.5 Kinetic Inductance

Kinetic inductance only occurs in alternating electric fields and can be treated as an additional series inductance. It is caused by the inertial mass of the charge carriers. According to the Drude model [26] the current in a normal conductor is described by Ohm's law:

$$\vec{J} = \frac{nq^2\tau}{m} \vec{E} = \sigma^{-1} \vec{E} \tag{1.60}$$

n is the charge carrier density, q the charge, τ the collision time, m the charge carrier mass and σ the conductivity. In an oscillating electric field of frequency ω the complex conductivity

is given by:

$$\sigma = \frac{nq^2\tau}{m(1+i\omega\tau)} = \frac{nq^2\tau}{m(1+\omega^2\tau^2)} - i\frac{nq^2\omega\tau^2}{m(1+i\omega^2\tau^2)} = \sigma' - i\sigma'' \tag{1.61}$$

The imaginary part is caused by the kinetic inductance. For a superconducting wire the kinetic inductance can be calculated by equating it with the kinetic energy of the Cooper pairs.

$$\frac{1}{2}(2m_e v^2)(n_s l A) = \frac{1}{2}L_k I^2 \tag{1.62}$$

$2m_e$ denotes the mass of a Cooper pair, v its velocity, n_s the cooper pair density, l the length of the wire and A its cross-section. This expression leads to:

$$L_k = \left(\frac{m_e}{2n_s e^2}\right)\frac{l}{A} \tag{1.63}$$

The total inductance L_{tot} of a superconducting wire is composed of the geometrical inductance L_g and the kinetic inductance:

$$L_{tot} = L_g + L_k \tag{1.64}$$

leading to:

$$f_0 = \frac{1}{2\pi\sqrt{(L_g + L_k)C}} \tag{1.65}$$

Mattis and Bardeen demonstrated that the quality factor of a resonator can be described by the ratio of kinetic inductance and geometrical inductance and the ratio of real and imaginary part of the conductivity [27]:

$$Q_i = 2\frac{L_g}{L_k}\frac{\sigma'}{\sigma''} \tag{1.66}$$

This is a function of temperature. It decreases with increasing temperature because of the generation of quasiparticles.

1.2.6 Losses due to Two Level Systems

According to theory the quality factor is supposed to increase with decreasing temperature. This principal behaviour can be observed in experiment down to temperatures of $\sim 0.2T_c$ [28]. The data also shows a saturation at a certain temperature where the quality factor does not increase anymore. This behaviour indicates that there is some other mechanism that dominates the loss at low temperatures. The mechanism has been identified as two level systems at the interface of superconductor and substrate. Although there are different models for the structure of these two level systems, it is still not clear which one applies. However, the dissipation due to two level systems is well understood [28, 29]. If the stored energy in the resonator is increased, more of these systems get saturated. This reduces their limiting effect on the quality factor. The loss caused by two level systems does not only depend on the value of the electric field,
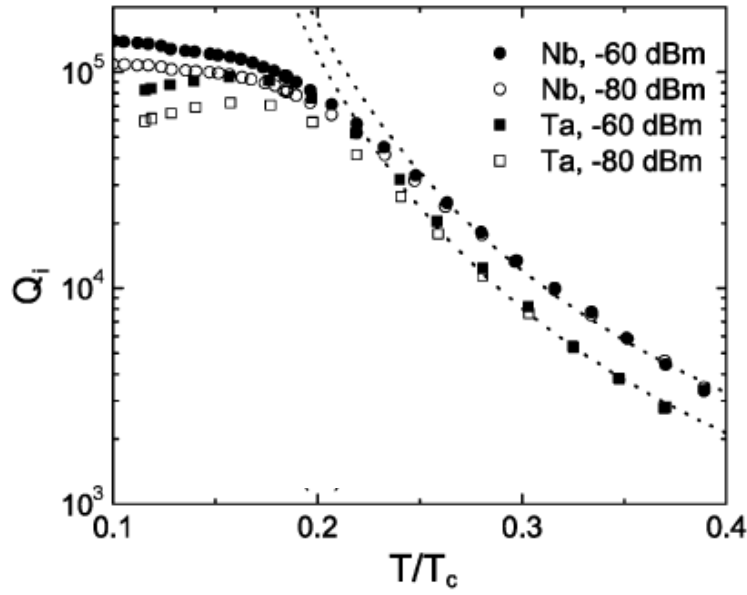
Fig. 1.5: Temperature dependence of the quality factor [28]. The dashed curve shows the quality factor predicted by theory.

which varies with the applied power. It depends on the electric field distribution, too, which is determined by the resonator geometry. The loss caused by two level systems is [30]:

$$\delta_{TLS,T=0} = \delta_0 F = \delta_0 \frac{\int\limits_{\Omega'} \epsilon_0 \epsilon_r |E|^2 \frac{1}{\sqrt{1+|E|^2/E_s^2}} d\Omega'}{\int\limits_{\Omega} \epsilon_0 \epsilon_r |E|^2 d\Omega} \tag{1.67}$$

δ_0 denotes the intrinsic loss of the material and F is the filling factor. E_s is the saturation field of the two level systems. The integral in the nominator is evaluated over the partial volume Ω' where the two level systems are arranged and in the denominator the integral is evaluated over the total volume Ω. The two level system losses also occur at higher temperature. In this regime, however, losses due to quasiparticles play the dominant role.

Chapter 2

Magnetic Fields in Hard Superconductors

As already pointed out in chapter 1.1.2, vortices enter the superconductor in the Shubnikov phase. If a transport current is flowing, these flux tubes experience a Lorentz force per unit length [19].

$$\vec{F}_L = \frac{\Phi_0}{c}\vec{I} \times \vec{e}_B \tag{2.1}$$

$\vec{e}_B$ is the unity vector in magnetic field direction and $\vec{I}$ the transport current. The Lorentz force accelerates the vortices in a direction perpendicular to the transport current. Bardeen and Stephen showed that for an ideal superconductor this motion is resisted by a viscous drag, which leads to an electrical resistance [31]. In reality there are always some imperfections in the crystal where the vortices get pinned. The vortices only move if the Lorentz force is bigger than the pinning force. In the following section we treat the superconductor as an ideal one, neglecting the vortex pinning.

2.1 The Bean Model

In 1962 Charles P. Bean published a model [14] for the magnetization of hard superconductors. In this model he assumes a filamentary structure capable of carrying a supercurrent up to a critical current density J_c. This critical current density depends on the magnetic field and becomes zero at the critical field. Furthermore he assumes that the interstices between the filaments are filled with a soft superconductor of critical field H_c. A cylinder of a hard superconductor with a magnetic field applied parallel to the cylinder axis is analysed. The radius R shall be much larger than the penetration depth. With these assumptions the cylinder completely expels the magnetic field in the Meissner phase. If the applied field H is larger than H_c, a circular current is flowing to a depth Δ:

$$\Delta = \frac{10(H - H_c)}{4\pi J_c} \tag{2.2}$$

The magnetic field distribution is then:

$$H_i = 0; \quad \text{for} \quad 0 \leq r \leq R\left(1 - \frac{H - H_c}{H^*}\right) \tag{2.3}$$

$$H_i = H - H^* \left(1 - \frac{r}{R}\right) \quad \text{for} \quad R \left(1 - \frac{H - H_c}{H^*}\right) \leq r \leq R \tag{2.4}$$

with

$$H^* = \frac{4\pi J_c R}{10} \tag{2.5}$$

If the magnetic field is larger than $H^* + H_c$, the magnetic field penetrates completely into the superconductor. The magnetic field distribution is then given by:
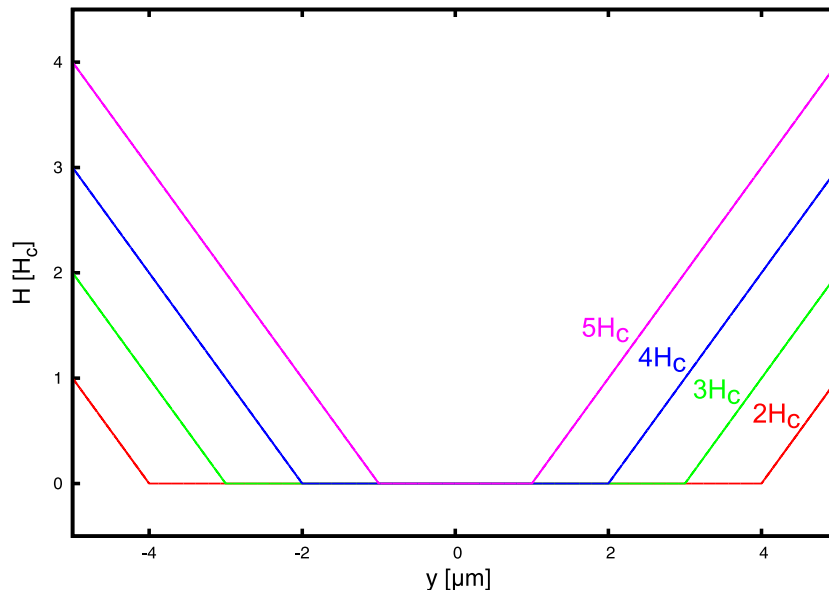
$$H_i = H - H^* \left(1 - \frac{r}{R}\right) \tag{2.6}$$

Fig. 2.1: Magnetic field distribution for magnetic fields from $2H_c$ up to $5H_c$ in the intersection of a hard superconductor according to the Bean model. The diameter is $10\mu m$, as is the strip width of the fabricated samples.

2.2 The Norris Brandt Indenbom Model

Brandt and Indenbom [16] developed the Bean model further, also taking into account the work of Norris [15]. On the one hand the Bean model applies to the magnetization for long cylinders. On the other Brandt and Indenbom calculate the flux distribution in a flat superconductor with a perpendicular magnetic field. The considered geometry is that of a long wire with $|x| \leq d/2$, $|y| \leq a$ and $|z| \leq \infty$, where $2a$ is the strip width and d the film thickness with $d \ll a$. The magnetic field distribution for such a wire is given by:

$$H(y) = \begin{cases} 0 & |y| < b \\ H_c \mathrm{arctanh} \dfrac{\sqrt{y^2 - b^2}}{c|y|} & b < |y| < a \\ H_c \mathrm{arctanh} \dfrac{c|y|}{\sqrt{y^2 - b^2}} & |y| > a \end{cases} \tag{2.7}$$

with

$$b = \frac{a}{\cosh(H_\alpha / H_c)} \tag{2.8}$$

$$c = \tanh\left(\frac{H_\alpha}{H_c}\right) \tag{2.9}$$

The flux distribution depends on the magnetic history. This equations only describe the field distribution correctly if the superconductor was in the so-called virgin state. This means that it did not experience a magnetic field before.
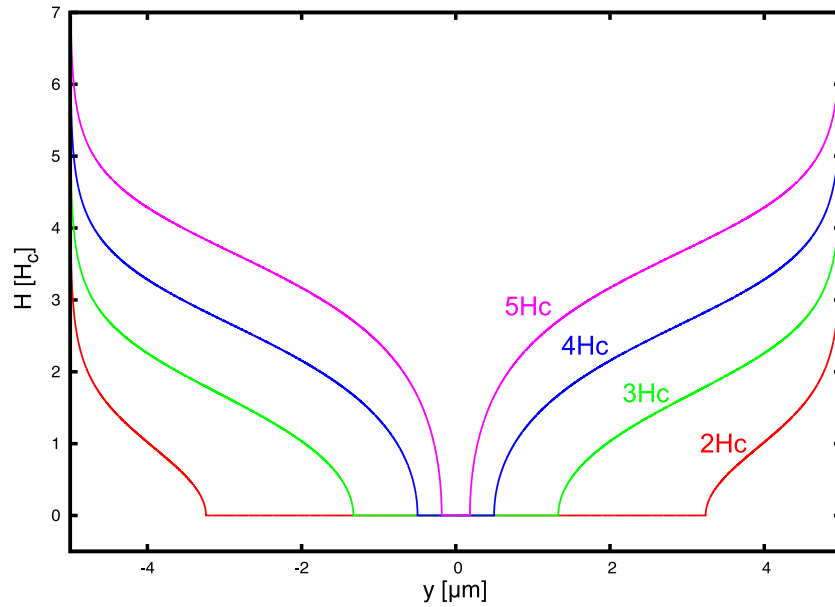

Fig. 2.2: Magnetic field distribution for magnetic fields from $2H_C$ up to $5H_C$ in the intersection of a hard superconductor according to the Brandt Indenbom model. The width is $10\mu m$, as is the strip width of our samples.

If the magnetic field is lowered again, the field distribution can be calculated by:

$$H(y) = H(y, H_0) - 2H\left(y, \frac{H_0 - H}{2}\right) \tag{2.10}$$

2.3 The Resonator Loss Model

Additional losses occur when superconducting resonators are operated in magnetic fields [8]. A possible mechanism for these losses has been given by Bothner *et al.* [1]. In this model,
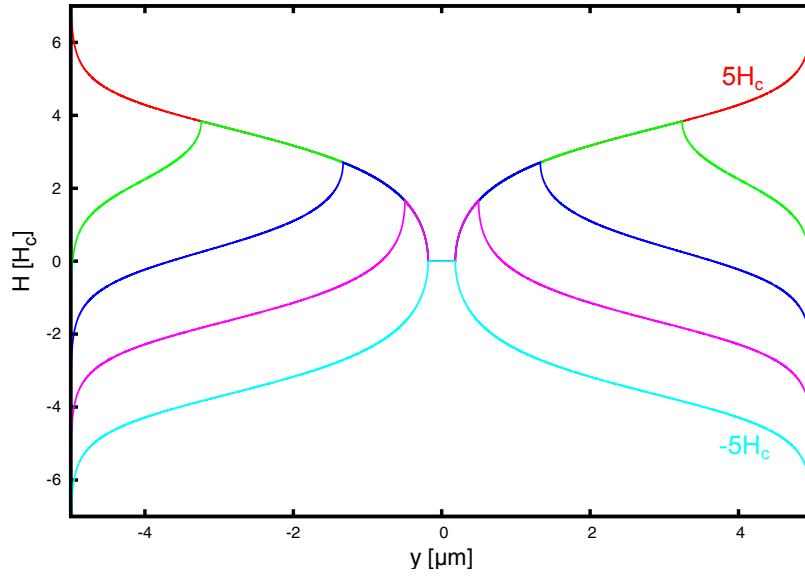
Fig. 2.3: Magnetic field distribution for magnetic fields from $5H_c$ down to $-5H_c$ in the intersection of a hard superconductor according to the Brandt Indenbom model. The width is $10\mu m$, as is the strip width of the samples we used.

an Abrikosov vortex is considered as a massless point-like particle under the influence of a Lorentz force $F_L = j\Phi_0$ with the oscillating current density $j = j_0\sin(\omega t)$. Each of this vortices dissipates energy. The released energy per oscillation is as follows:

$$\Delta E = \int_0^T F_L v dt \propto \int_0^T j(y)^2 dt \propto j_0^2 \tag{2.11}$$

This integral is proportional to the quadrature of the current, since the Lorence force and the average velocity are both proportional to it. If we now consider all the vortices in the superconductor, we have to sum up over all of them.

$$\Delta E_{total} = \sum_i \Delta E \propto \sum_i j(y_i) \tag{2.12}$$

As there are many vortices in the superconductor we can approximate them as a continuum represented by the magnetic field distribution. Furthermore we consider the current to be constant over the oscillation range. With this assumption the dissipated energy can be described by:

$$\Delta E_{total} \propto \sum_i \Delta E \propto \int_{-a}^a |B(y)|(j(y))^2 dy := \delta_e \tag{2.13}$$

The expression δe is proportional to the additional losses due to vortices δ_m. For the following calculations, we consider the current and magnetic field distribution to be independent of each other. We neglect the fact that magnetic fields induce currents and vice versa [1]. The current

distribution in a superconducting wire is given by:

$$j(y) = \frac{I}{K(\frac{a}{w})w(\sqrt{\zeta(y)}}$$

(2.14)

with

$$\zeta(y) = \begin{cases} \frac{\lambda_{eff}}{S}\left(1 - \left(\frac{a}{w}\right)^2\right) & 0 \leq \frac{a}{2} - |y| < \lambda_{\text{eff}} \\ \left(1 - \left(\frac{2y}{w}\right)^2\right)\left(1 - \left(\frac{2y}{a}\right)^2\right) & |y| \leq \frac{a}{2} - \lambda_{\text{eff}} \end{cases}$$

(2.15)

w_g is the gap width and $w = a + 2w_g$ is the distance between the groundplanes. K is the complete elliptic integral and I the overall current. λ_{eff} is the effective penetration depth given by:

$$\lambda_{\text{eff}} = \lambda_L \coth\left(\frac{d}{\lambda_L}\right)$$

(2.16)

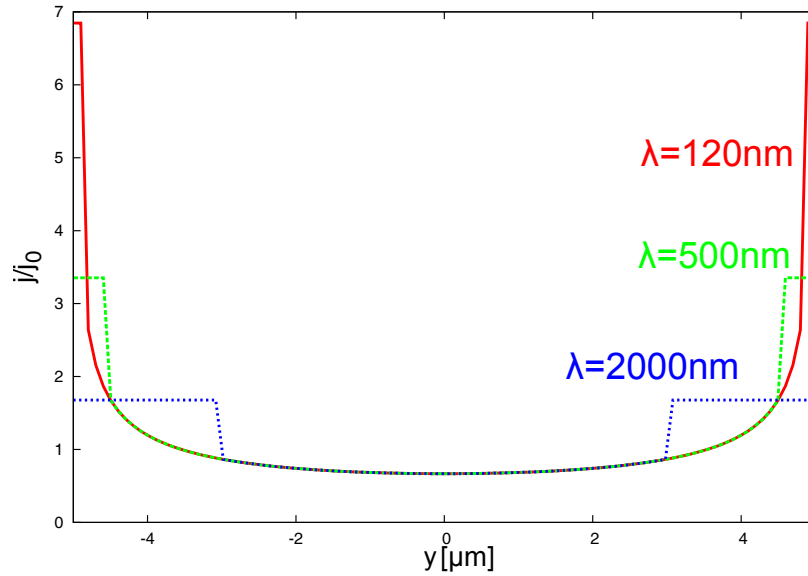Magnetic hysteresis curves can be obtained by integrating over the product of magnetic field

Fig. 2.4: Current distribution for different London penetration depths. The width is $10\mu m$, as is the strip width of our fabricated samples.

and the quadrature of current density for different applied magnetic fields. They show different shapes, depending on the applied field and the current distribution, but the principal features are the same for all these curves. Figure 2.5 illustrates such a magnetic hysteresis curve.

2.4 Magnetic Hysteresis of the Resonance Frequency

The models used so far did not consider the magnetic field entering the superconductor in the Meissner phase. In this phase the magnetic field is shielded exponentially from the interior of the superconductor. The penetrated magnetic field also leads to losses. No hysteresis effects
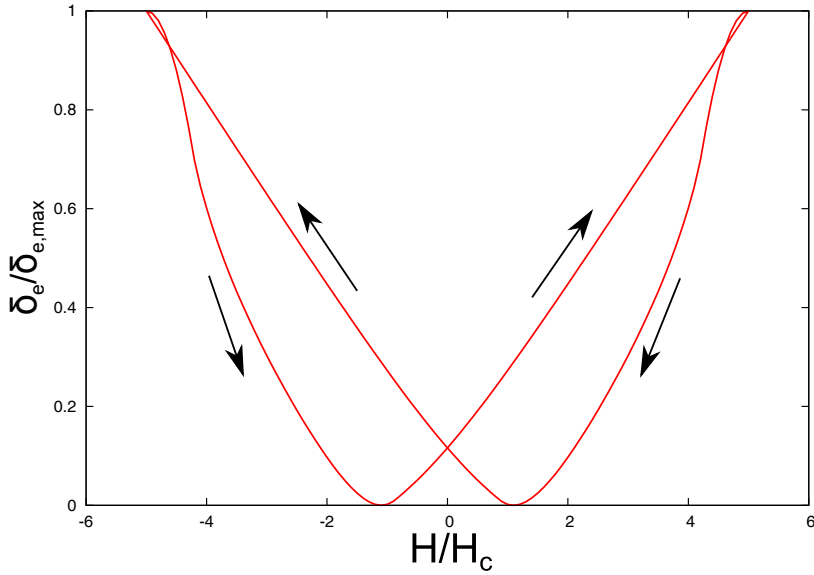
Fig. 2.5: Calculated losses for a sweep from $5H_c$ to $-5H_c$ and back according to the resonator loss model. The London penetration depth for this simulation was $360nm$ and the strip width $10\mu m$.

occur since only the amplitude changes and the distribution stays the same. Not only can changes in loss be observed, but variations in resonance frequency can be detected, too [9]. This effect can be explained by considering the proportionality of magnetic field and screening current. The linear relation breaks down because of pair breaking induced by the velocity field [32]. This phenomenon evokes a change in the Cooper pair density. As a result the effective penetration depth λ_{eff} is changed. The kinetic inductance L_k and thus the resonance frequency change as well:

$$\lambda_{\text{eff}}(T,H)^{-1} = \lambda(T)^{-1}\left(1 - \frac{1}{3}\alpha(T)\left(\frac{H}{H_0(T)}\right)^2\right) \tag{2.17}$$

The change in resonance frequency can be observed directly in experiment [9]:

$$f(T,H) = f(T,0)\left(1 - \beta(T)\frac{L_k(T,0)}{L_{total}}\frac{H^2}{H_c^2}\right) \tag{2.18}$$

This correlation explains changes in resonance frequency for superconductors in the Meissner phase. Nevertheless, it can not provide an explanation for hysteresis effects, as have been observed, too [1]. Such effects only take place in the Shubnikov phase and can be explained in the case of the field entering the superconductor is taken into account. Instead of the squared applied field, the integral over the squared entered field is used, leading to

$$f(T,H) = f(T,0)\left(1 - \beta(T)\frac{L_k(T,0)}{L_{total}}\frac{\int H^2\,dy}{2aH_c^2}\right) \tag{2.19}$$

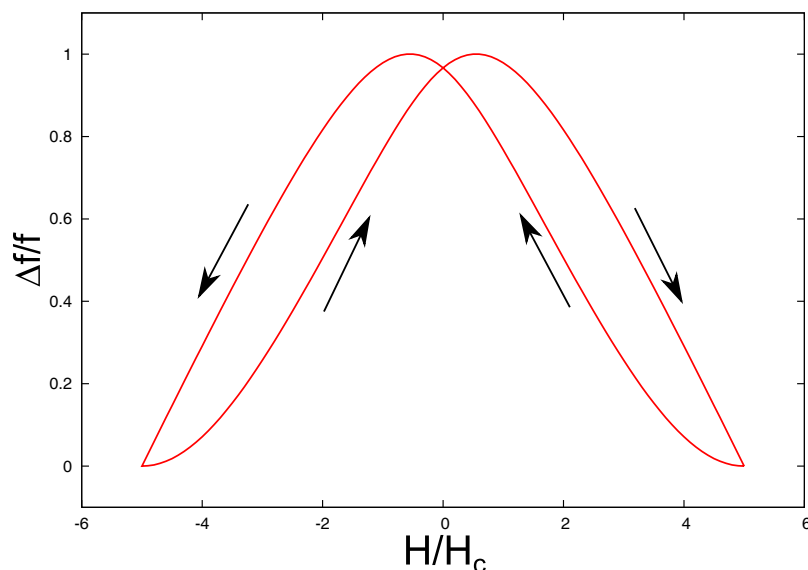With this formula hysteresis effects in resonance frequency can be explained in principle. Fig-

Fig. 2.6: Calculated change in resonance frequency for a sweep from $5H_c$ to -$5H_c$ and back according to equation (2.19). The London penetration depth for this simulation was 120 nm and the strip width was 10μm. The arrows indicate the sweep direction.

ure 2.6 shows such a resonance curve. At first the resonance frequency shifts to lower values. When the absolute value of the magnetic field is reduced the resonance frequency rises again. After passing zero magnetic field it reaches a maximum. This behaviour does not match the experimental one in this and other works [1]. A reason for the discrepancy is that this formula does not take into account the different local contributions of the kinetic inductance.

The kinetic inductance describes the response of the charge carriers to an electromotive force. In a superconductor all the charge carriers that account for the current are localised at the edges. Only these charge carriers contribute to the kinetic inductance. This distribution has to be considered when changes in the kinetic inductance caused by magnetic fields are calculated.

$$f(T,H) = f(T,0) \left(1 - \beta(T) \frac{L_k(T,0)}{L_{total}} \frac{\int H^2 I \, dy}{2a I_{total} H_c^2} \right) \qquad (2.20)$$

The curves calculated with this formula all show the same characteristics. After reducing the magnetic field the resonance frequency rises tremendously until its maximum value.
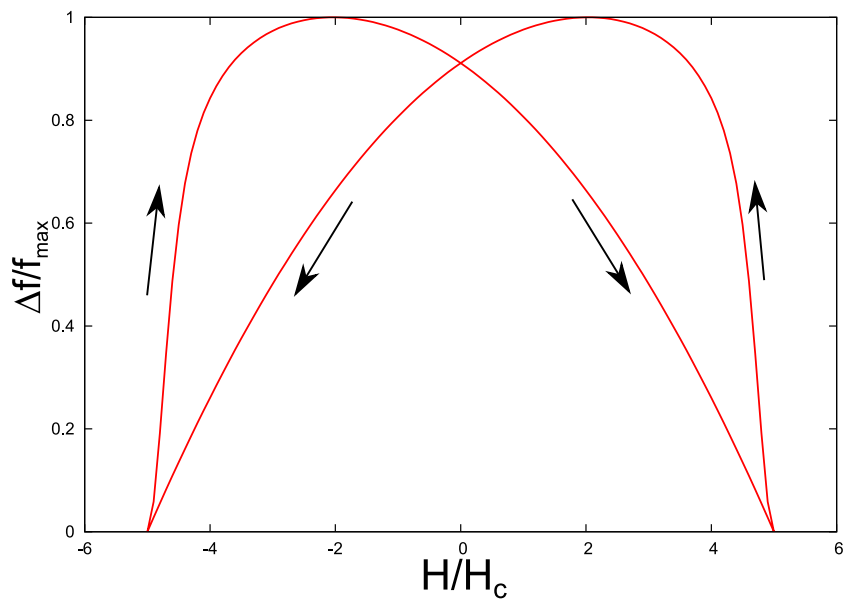
Fig. 2.7: Calculated change in resonance frequency for a sweep from $5H_c$ to -$5H_c$ and back according to equation (2.20). The London penetration depth for this simulation was 120 nm, the strip width 10 μm. The arrows indicate the sweep direction.

Chapter 3

Fabrication

An approach of understanding magnetic hysteresis effects in microwave resonators better is based on the investigation of hysteresis effects for different parameters. Some of these parameters are extrinsic and can be changed in experiment, for example, temperature, applied microwave power or the magnetic field. Others are intrinsic parameters of the fabricated samples, for instance film thickness, strip width, coupling strength or resonator geometry. Some parameters are material specific, such as the London penetration depth and the superconducting gap and can not be chosen arbitrarily. The whole patterning of the chips was done at our group, which provided the possibility to choose the sample parameters according to our research interest. In this chapter the whole design and fabrication process is described. It ranges from thin film deposition and designing the chip to producing a chromium photomask and etching the chips. In Appendix A the parameters for the fabrication steps are listed.

3.1 Material

We chose the material titanium nitride (TiN) because it has some promising properties. The coherence length of TiN is 39 nm [33] and its penetration depth 275 nm [34]. So its GL parameter κ, which was introduced in equation 1.7, is 7. It is bigger than $\frac{1}{\sqrt{2}}$ and hence titanium nitride is a magnetically hard superconductor. This ensures that magnetic hysteresis effects can be observed at all. Furthermore it is a material with a high kinetic inductance, which is crucial for the analysis of the change in resonance frequency. Another fundamental aspect for our research is that TiN exhibits very low losses. Internal quality factors up to 10^7 have been demonstrated at millikelvin temperatures and high photon numbers [35].

This characteristic makes titanium nitride a very interesting material for quantum information processing. TiN is mechanically very stable and a chemically inert material. It has a low surface oxidation rate and almost no degradation over time. For our purposes it means that we can still use the resonators long time after fabricating them. Because of these features titanium nitride is also used as a coating for tools. Its transition temperature depends on its composition, reaching values of up to five Kelvin [35]. This is a convenient tool if TiN resonators are used for photon detection. For us it means that we have to investigate the hysteresis effects at temperatures well below the boiling temperature of helium at atmosphere
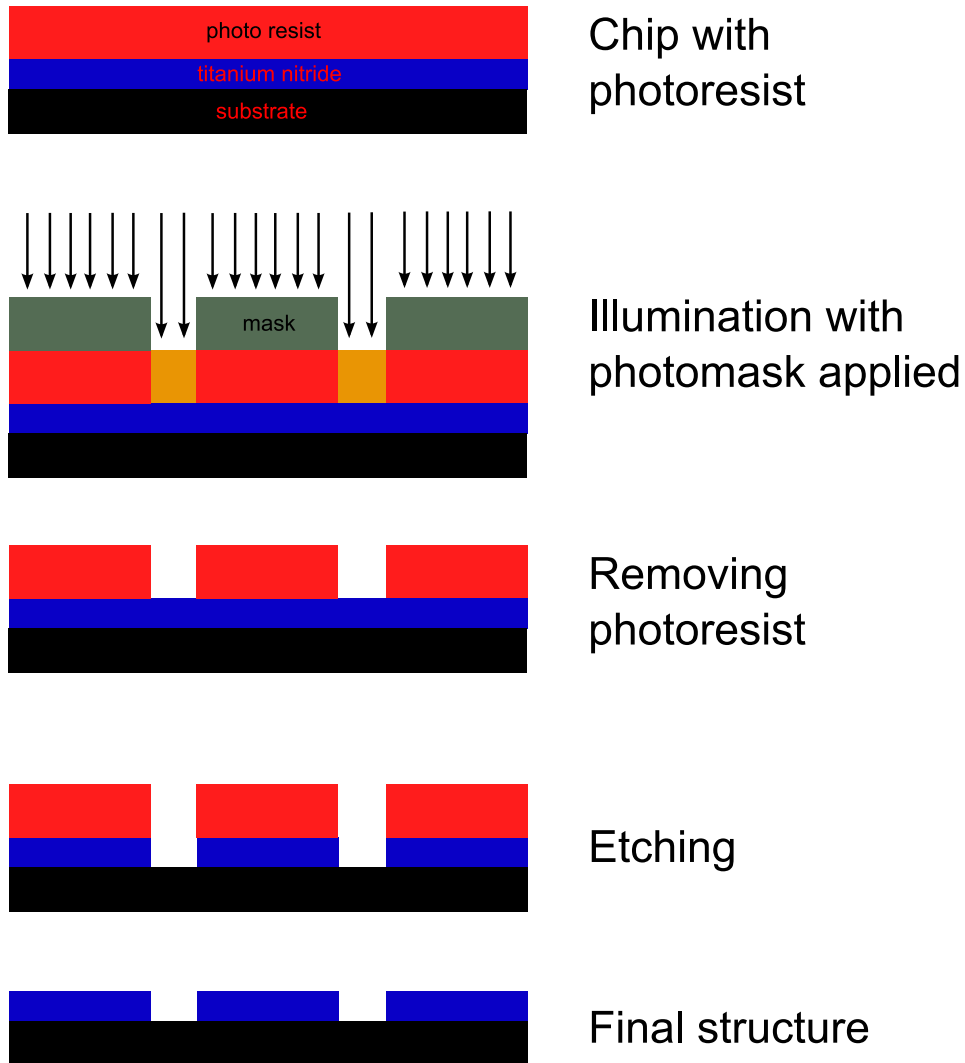
photo resist	
titanium nitride	Chip with photoresist
substrate	

mask	Illumination with photomask applied

	Removing photoresist

	Etching

	Final structure

Fig. 3.1: Fabrication process

pressure. Not only is the choice of the superconductor of relevance, but the substrate material is essential, too. It has been demonstrated that for titanium nitride low losses can be achieved by using nitrided intrinsic silicon as substrate [34].

The films we structured in this work were deposited at NIST. 40nm of TiN were reactively dc sputter deposited onto intrinsic Si(100). Before deposition, the silicon oxide on the wafer was chemically removed and the surface was terminated with hydrogen. Moreover, a very thin film of SiN was formed on the hot sample right before sputtering. The TiN in this sputtering process is structured in a (200)-geometry [34]. We received the wafer protected with photoresist and diced into six $(5mm)^2$ chips.

3.2 Sample Design

In this work resonators of different designs were fabricated. They include quarter and half wavelength resonators as well as parallel lumped LCs. Some of these designs were provided by Martin Weides. One chip design containing 24 lumped LC resonators coupled to one feedline was created by using the software L-edit [36].
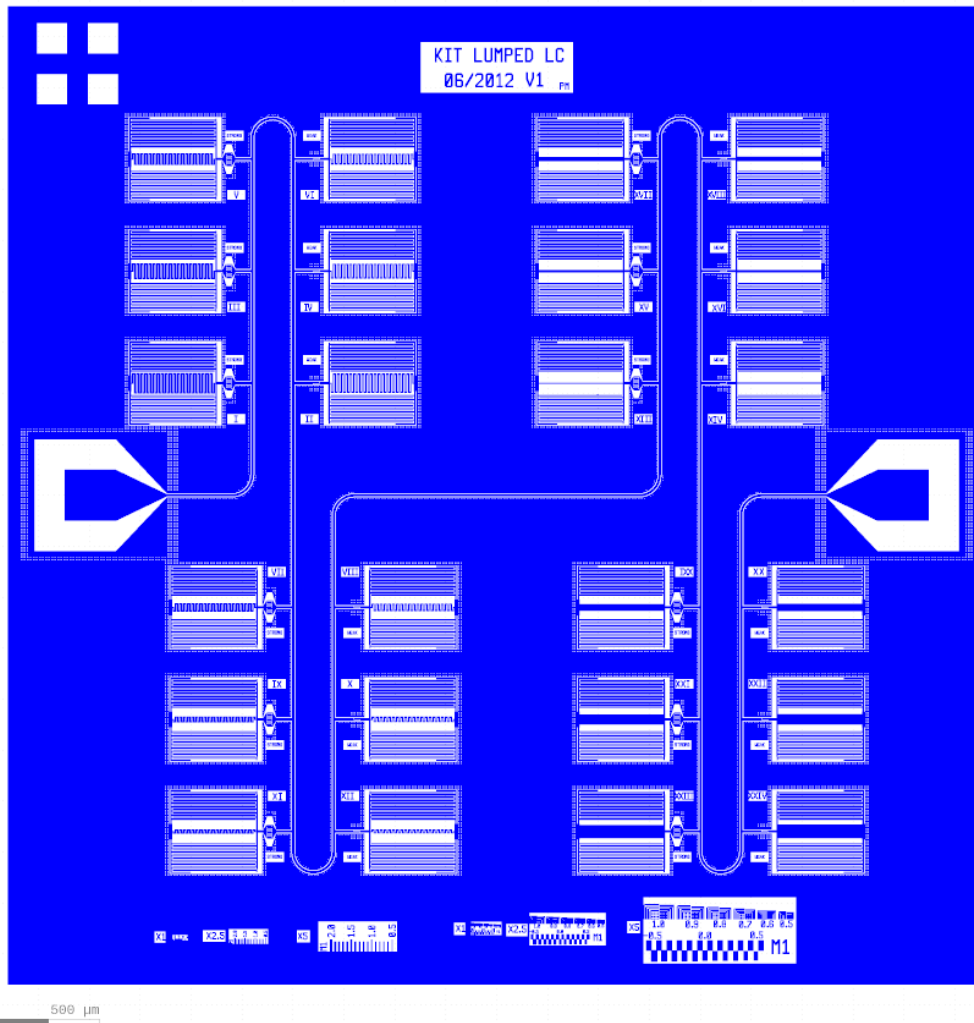

Fig. 3.2: $(5\text{mm})^2$ chip design with 24 LC resonators. The blue regions shall be superconductor, the small dots around the structures are flux traps.

The width of the coplanar waveguide feedline was chosen to be $10\mu m$ and the gap width to the ground planes was $6\mu m$, which leads to an impedance of 50 Ω. We chose the resonance frequencies to range equidistantly from 4.5 GHz up to 12.3 GHz. There are twelve pairs of resonators. Each pair consists of a strongly coupled and a weakly coupled resonator. The strongly coupled resonators have a slight offset in resonance frequency so that the resonators

can be distinguished. The designed coupling quality factors are $Q_{c1} = 5000$ and $Q_{c2} = 100000$. We did not know from the beginning how big the quality factors were going to be and because of this used different coupling strengths. If Q_c is much smaller than Q_i, the total quality factor is dominated by the coupling, which makes it very hard to identify Q_i.
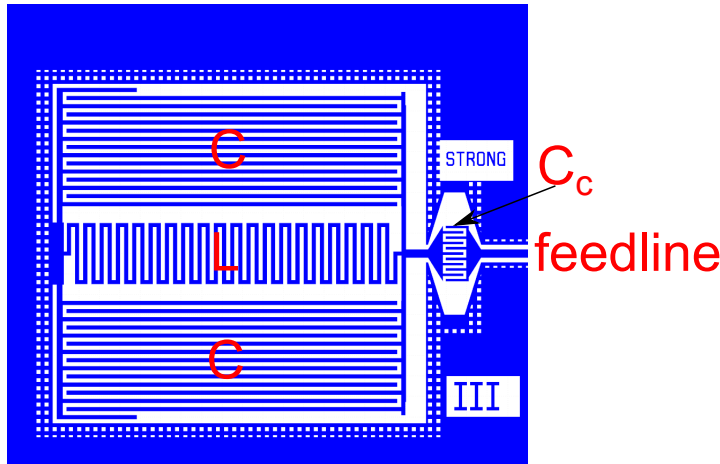

Fig. 3.3: LC resonator design with $f_0 = 5.1$GHz. The L in the middle denotes the inductor and the C above and below symbolise the capacitors. C_c stands for the capacitor which couples the resonator to the feedline on the right. The blue regions shall be superconductor, the small dots around the structures are flux traps.

In this design the frequency of the resonators was changed by adjusting the meandered inductance and keeping the capacitance constant. The inductance was changed by either altering its length or its strip width. We applied a pattern of quadratic flux traps of a length of $5\mu m$ around all structures. This pattern prevents magnetic flux from entering the transmission line or the resonators. The big contact pads at the ends of the feedline provide a bigger area for connecting it to the center conductor.

Each resonator was analysed separately with the Sonnet simulation software [37] in order to calculate the resonance frequency. This software solves the Maxwell equations at certain frequencies and extrapolates the transmission properties for a defined frequency spectrum. It treats the superconductor as an ideal one without any losses. The coupling quality factor can also be estimated with the calculated transmission. Therefore the difference of the resonance frequencies Δf at a transmission of -3dB is measured (see figure 3.4). The loaded quality factor satisfies the following equation:

$$Q_L = \frac{f_0}{\Delta f} \tag{3.1}$$

Since the internal quality factor in this calculation is infinite, the coupling quality factor equals the loaded one.
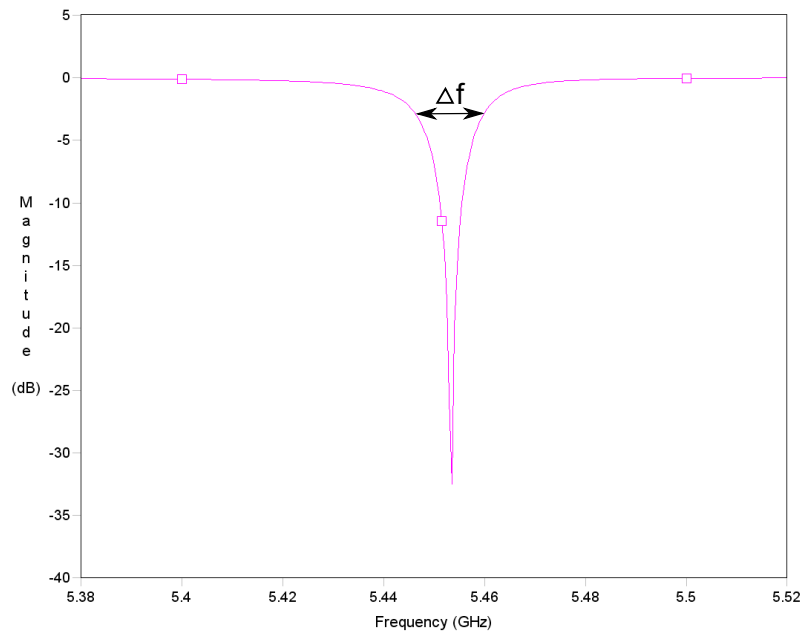
Fig. 3.4: Transmission S_{21} of an LC resonator modeled by sonnet. The squares indicate the frequencies where the software actually solves the Maxwell equations. Δ f is the difference of the resonances at -3dB.

3.3 Patterning

Patterning the chip is done with optical lithography using positive photoresists and reactive ion etching. Photoresists are photoreactive polymers. They consist of three components: a resin, a photoactive compound and a solvent [38]. The resin serves as a binder and establishes the mechanical properties. The function of the solvent is to keep the resist liquid. When the photoresist is heated, the solvent evaporates and the photoresist becomes solid. The photoactive compound reacts under illumination of certain wavelengths, which changes the solubility. As a consequence, only the photoresist in the light-exposed regions gets washed away when the photoresist is developed. This type of resist is called positive resist. For a negative resist only the illuminated regions remain by.

3.4 Chromium Photomask

The first fabrication step is to create a chromium reticle using optical lithography. Writing the photomask was done with a 2D laser lithography tool (Heidelberg DWL66). We selected photomasks that are $(100mm)^2$ in area. For this reason, enough area for many chip designs could be provided. Since the chips are $(20mm)^2$ in size, we decided to structure four identical designs on the mask. Although we need only one three times three array in order to structure the chips, it is convenient to work with the whole space of the mask. In this array we implemented the lumped LC design three times, twice a $\frac{\lambda}{2}$-design and two $\frac{\lambda}{4}$-designs with different resonator

geometries. We chose a fused quartz photomask of 2.3 mm thickness covered with 530 nm AZ518 photoresist. In a first step the photomask is fixed on a moveable plate under a laser of 420 nm wavelength. Then the plate rasterises until all the desired area has been positioned directly under the laser. The laser gets blanked off for areas that shall not be exposed. The illuminated photoresist was removed after exposure with bathing the mask in microdeposit MF 319 for 60 seconds. Afterwards the chromium was etched away by dipping the mask in chrome etch 18 for 60 seconds. In a final step, the residual photoresist was removed with acetone.

3.5 Spin Coating

A homogenous distribution of the photoresist is needed for structuring. This can be realised by rotating the chip very fast. The achieved film thickness depends on the viscosity of the resist and its adhesion to the substrate as well as on the rotation speed. The photoresist is distributed on the chip homogeneously using a spin coater. The photoresist we used is S1805, which is a positive resist. About 80% of the surface were covered with resist before spinning the chip. We used two different spinning speeds; at first, 500 rpm to spread the fluid over the whole surface. In a second step the chip was rotated with 4000 rpm to attain the desired resist thickness of 500nm. Afterwards the chip is heated on a hot plate for 60 seconds at a temperature of 115 °C.

3.6 Mask Aligning

The next step is to illuminate the desired area of the chip with a mask aligner. Therefore the chip is located under the photomask and it is illuminated by a mercury-vapor lamp. The line spectrum of mercury shows three peaks in the range where photoresists usually react. These are the g, h and i-line of 436, 405 and 320 nm wavelength, respectively. A 6 inch mask aligner with a 350 W Hg-bulb emits approximately 20-30 mW/cm^2 for these three wavelengths [39]. This Intensity can change over the lifetime of a Hg-bulb.

Different modes can be chosen for aligning the chip to the photomask. We decided us for the hard contact mode, in which the chip is pressed against the photomask with a certain pressure. The resolution achieved by application of this mode is best, for there is no spacing between mask and chip. Unfortunately, a disadvantage of this technique is that the photomask might get damaged or dirty by pressing the chip to it. After alignment, the mask area is flood exposed with light from the mercury-vapor lamp. We determined an optimised exposure time of five seconds at a power of 275 W. Then, the illuminated photoresist was removed by bathing the mask in the developer microdeposit MF 319 for 60 seconds. We used a Karl Suss mask aligner for this fabrication step.

3.7 Reactive Ion Etching

There are several ways of etching a substrate. Wet etching is based on chemical reactions, whereas for ion mill etching the impulse of the ions is transferred to the substrate and the atoms get catapulted out. Reactive ion etching is a combination of both. Etching the TiN away can be done in different ways, for instance, ion mill or reactive ion etching. Previous studies by Sandberg et al. have found out a quality factor dependency on the etching method [13]. All pictures shown in figure 3.5 indicate that not only TiN, but also the substrate is
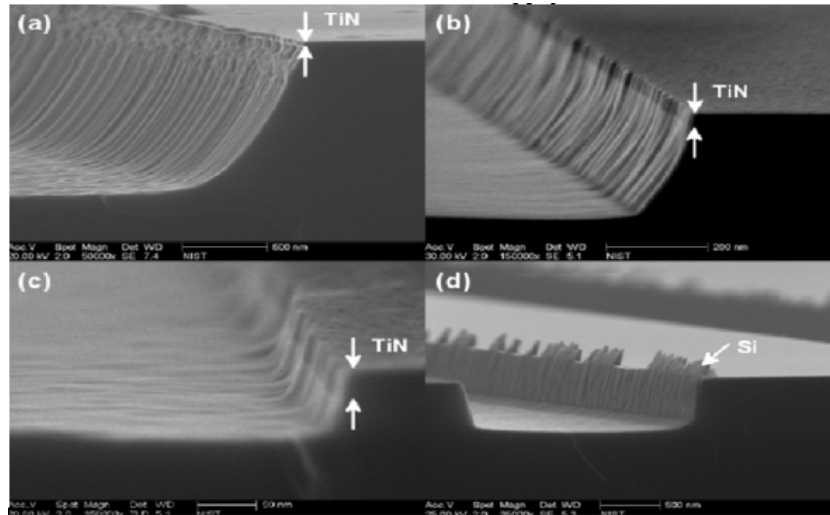

Fig. 3.5: SEM Pictures of TiN on intrinsic silicon [13]. a) shows a fluorine etched sample, b) and c) exhibit chlorine etched ones and c) was structured with Argon ion milling.

removed. Argon ion milling leads to a redeposition of the silicon substrate at the edges of the film. These trenches cause additional two level systems. For reactive ion etching, processes based on different materials can be used, such as fluorine and chlorine etching. Fluorine etching processes have a high material selectivity. The etching speed for silicon is 20 times higher than for TiN, which leads to deep trenches in the substrate. In the picture for the fluorine based process even an undercut can be observed. These trenches lower the filling factor (see equation 1.66) and so the loss of the resonator [30].

We chose reactive ion etching with a fluorine etching process based on SF6 to structure the resonators. A chemically reactive plasma is created by applying a high voltage between the electrodes of the plasma chamber. The gas molecules are accelerated and ionised. This leaves behind positive and negative ions as well as free electrons and radicals. In an SF6 plasma the following breakup reactions take place [40]:

$$SF_6 + e^- \longrightarrow SF_4 + F + F^*$$
$$SF_6 + e^- \longrightarrow SF_4 + F_2^{(R)}$$
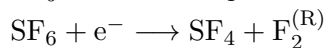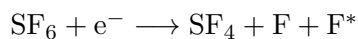
F^* stands for excited fluorine, a radical, and $F_2^{(R)}$ is a fluorine molecule in a high lying Rydberg state. Of course these products can recombine again. The result is an equilibrium where only a very small fraction of the atoms and molecules is ionised, in the range of one ion per 10^4 to 10^6

neutral ones [38]. The ions get accelerated towards the sample, but the transferred momentum is insufficient to break off the structures. Instead, a low reactive surface is made more reactive by damaging it. The ions can provide energy the etch products need to desorb from the surface as well [38]. We etched the chip for 8 minutes with an etch rate of 6 nm/min. Afterwards the photoresist was stripped off and the chip was diced into small $(5\text{mm})^2$ ones.
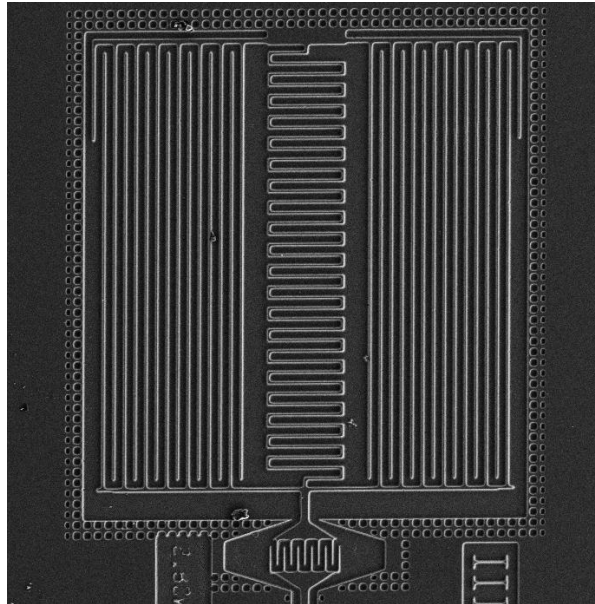

Fig. 3.6: SEM picture of a lumped element resonator. The meandered inductance can be seen in the middle. The long finger capacities are shown on the right and left part of the picture. The coupling capacitance to the feedline is shown at the bottom. A pattern of flux traps surrounds the structures.
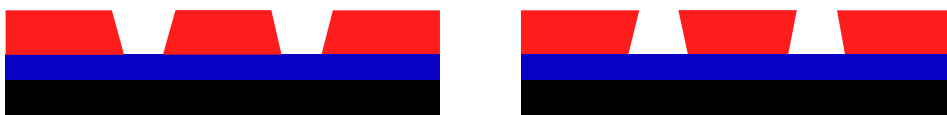

Fig. 3.7: Photoresist profile for a positive (left) and negative resist (right)

As can be observed in the figures 3.6 and 3.8, the structures are thinner than designed. They also show a rather tapered profile in vertical direction. Since this lithography process consists of many steps, there are different possible reasons for the discrepancy between design and on-chip structure. The resolution of the chip can at best be as good as the one of the reticle. For the photomask, the resolution is determined by the laser profile and its intensity as well as by the chemical etching process. For the chips fabricated in this work, we used a reticle that was produced with the 10 mm writing head. We furthermore structured a photomask with a 2 mm writing head, which showed a higher resolution. In addition, the final resolution of the chip depends on the photoresist profile and the etching parameters. The tapered profile can be explained by considering the photoactive compound loss. The shape of the residuals of a photoresist with less photoactive compound is illustrated in figure 3.7. Such profiles arise
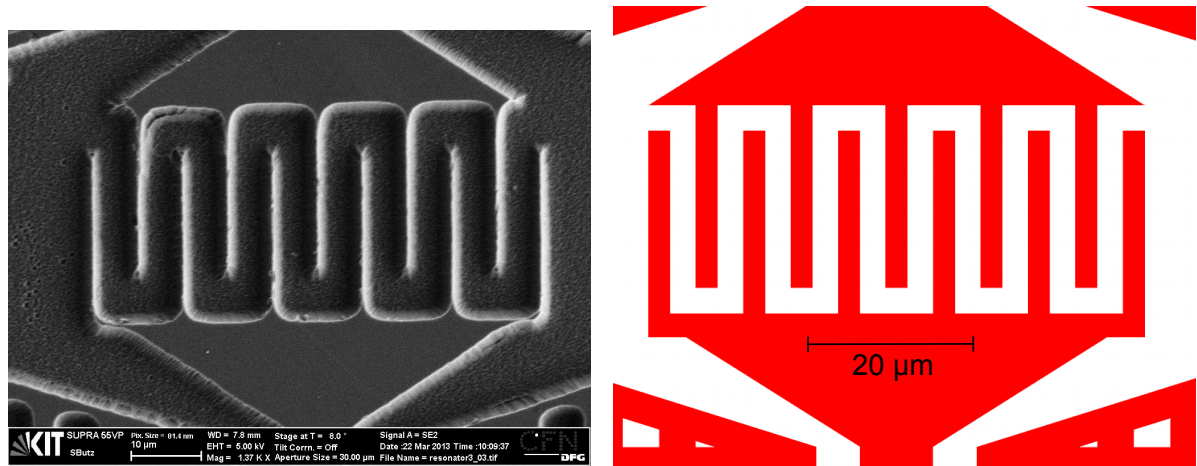
Fig. 3.8: closeup of the fabricated and the designed coupling capacitance.

on the chip when the resist is etched away, too. To get an ideal etching process a photoresist profile like in figure 3.1 is needed. A stronger underetching could be obtained with wet etching, because the etching speed does not depend on the direction for this process.

Chapter 4

Measurement Setup

4.1 Resonators

We investigated the magnetic behaviour of $\frac{\lambda}{4}$-resonators in an array of 14 resonators. The resonance frequencies were designed to range equidistantly from 4 to 10 GHz. Each of these resonance frequencies was implemented with two resonators of different coupling strengths; one with $Q_{c1} = 5000$ and the other one with $Q_{c2} = 250000$. Microscope images showed that three of the resonators are broken. The broken resonators are the weakly coupled ones with resonance frequencies of 5, 6 and 7 GHz.
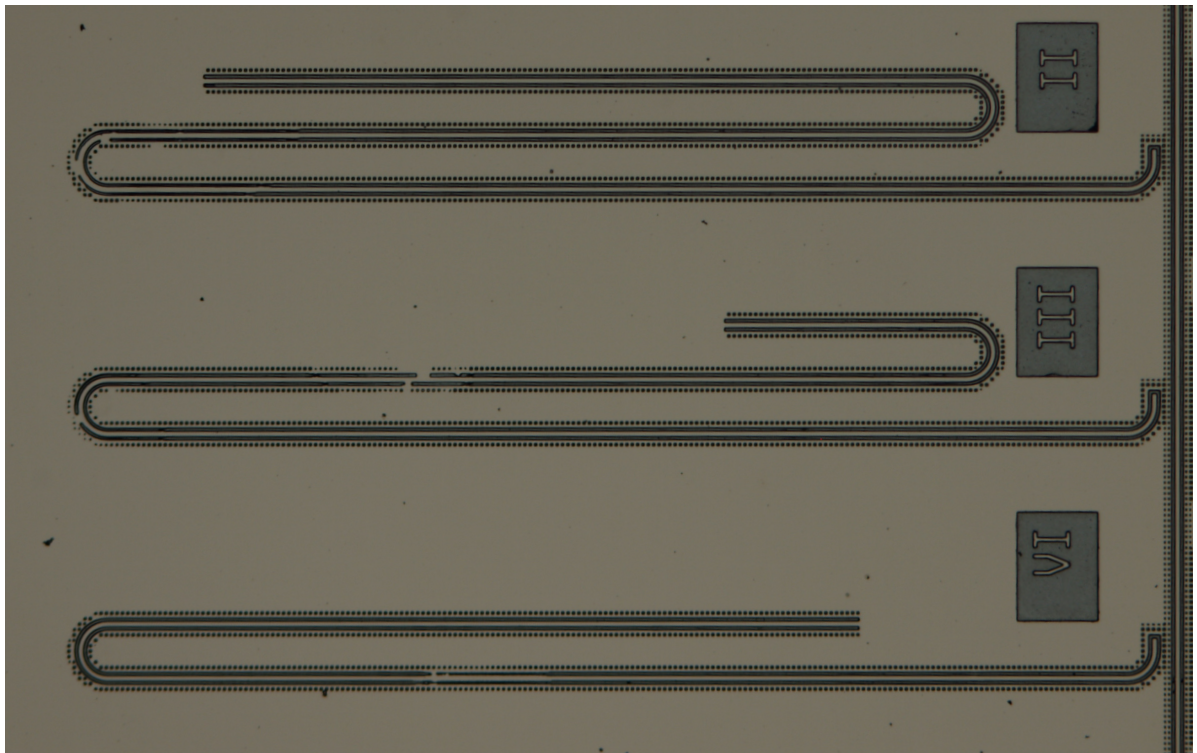

Fig. 4.1: Microscope image of the broken resonators.

4.2 Helium 3 Setup

The expected critical temperature of our sample lies at about four kelvin. If we want to reach high quality factors, the resonators need to be operated at a temperature well below T_c. Therefore liquid helium with a boiling temperature of 4.2 K at atmosphere pressure is insufficient. By reducing the pressure temperatures down to 1 K can be reached. To reach lower temperatures the isotope ^{3}He can be used. It is very rare and expensive. Hence, it needs to be operated in enclosed systems. Temperatures below 300mK can be achieved by pumping on it. We used such a helium 3 system for this work.

The sample is glued to a printed circuit board which is inserted in a sample box. To connect the feedline to the center conductor three bonding wires are applied on each side. The ground planes of the printed circuit board and the chip are connected with bonding wires as well. The sample box is fixed to the end of a dipstick. A so-called 1-K pot, a small container which is continuously filled with helium from the main bath and an enclosed helium 3 system is mounted on this dipstick. We only pump on the 1-K pot, instead of pumping on the main bath of the dewar. Pumping on the helium 3 is done with a charcoal sorption pump. Charcoal adsorbs helium at low temperatures, but desorbs it at temperatures above 20 K [41]. This means that the sample temperature can not remain at 300 mK all the time. Instead the helium 3 needs to be cycled. Firstly, we pump on it until all the helium is absorbed. Secondly, the pump is heated until the helium desorbs again. With this setup it is possible to remain at the base temperature for about eight hours, after what the charcoal pump needs to be heated for three hours. The dipstick is inserted in a can filled with liquid helium with a capacity of 100 litres.
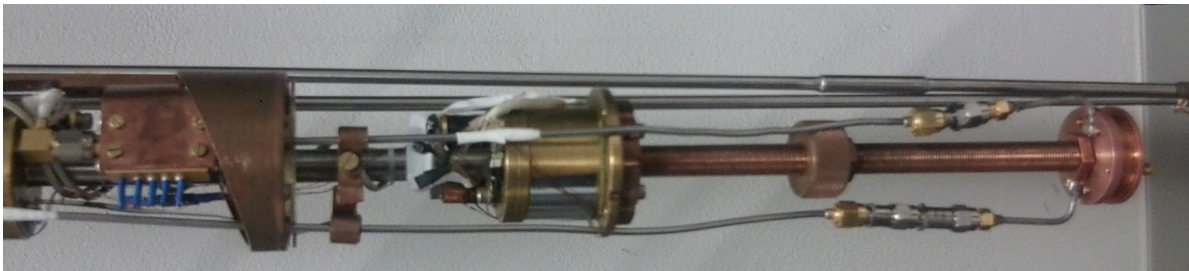

Fig. 4.2: Lower part of the of the helium 3 dipstick. The cables guide the current down to the sample box where the chip is located. The big cylinder in the middle is the helium 3 pot and the device on the left side where the small blue cables are inserted is the HEMT.

Measuring is done with a two port vector network analyser (VNA) with a spectrum up to 20 GHz. The VNA ports are connected to the sample via 50 Ω coaxial microwave cables. There are several attenuators applied at different temperature stages, and a high-electron-mobility transistor (HEMT) at the 4 K stage after the sample, as illustrated in figure 4.3. The function of the HEMT is to amplify the signal. The attenuators reduce the thermal noise from the higher temperature stages. We measured the temperatures at the 300 mK stage, the 1-K pot
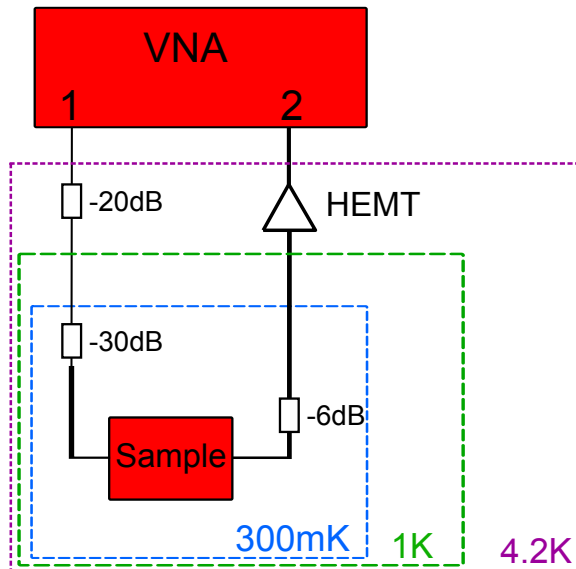
Fig. 4.3: Schematic microwave setup.

and the charcoal pump. At the 300 mK stage there is a heater applied, which can be regulated with a proportional-integral-derivative controller. The whole setup is not directly inserted in the liquid helium, but shielded by a copper cylinder. The air in this cylinder gets pumped out to get a better insulation. A magnetic shield is not applied. This means that the sample is affected by the external magnetic field. The vertical component of the earth magnetic field in Karlsruhe is 40 μT. We expect that this additional field shifts the magnetic hysteresis curves. The magnetic field is generated by a superconducting magnetic coil and points in vertical direction. It causes a magnetic field of 54 mT/A. The current source for the magnetic field and the VNA can be controlled by a PC via QtLab. The magnetic field was not measured directly, but calibrated via the current applied to the coil.

4.3 Fitting Process

The complex transmission S21 through a feedline coupled to a $\frac{\lambda}{4}$-resonator can be described by [25, 42, 43]:

$$S_{21} = ae^{i\alpha}e^{-2\pi if\tau}\left(1 - \frac{Q_L}{|Q_c|}\frac{e^{i\Phi}}{1 + 2iQ_L(\frac{f-f_0}{f_0})}\right) \tag{4.1}$$

a is a factor describing attenuation and amplification of the system; α stands for a constant phase offset, and τ denotes the cable delay. The phase Φ takes into account the mismatch between input impedance and output impedance of the resonator. This formula describes a circle if the imaginary part is plotted versus the real part.

Figure 4.4 shows the data after normalisation. The diameter of the circle is $\frac{Q_L}{|Q_c|}$. It is rotated to the real axis by the angle Φ. These values are calculated by the circle fit. In contrast, the
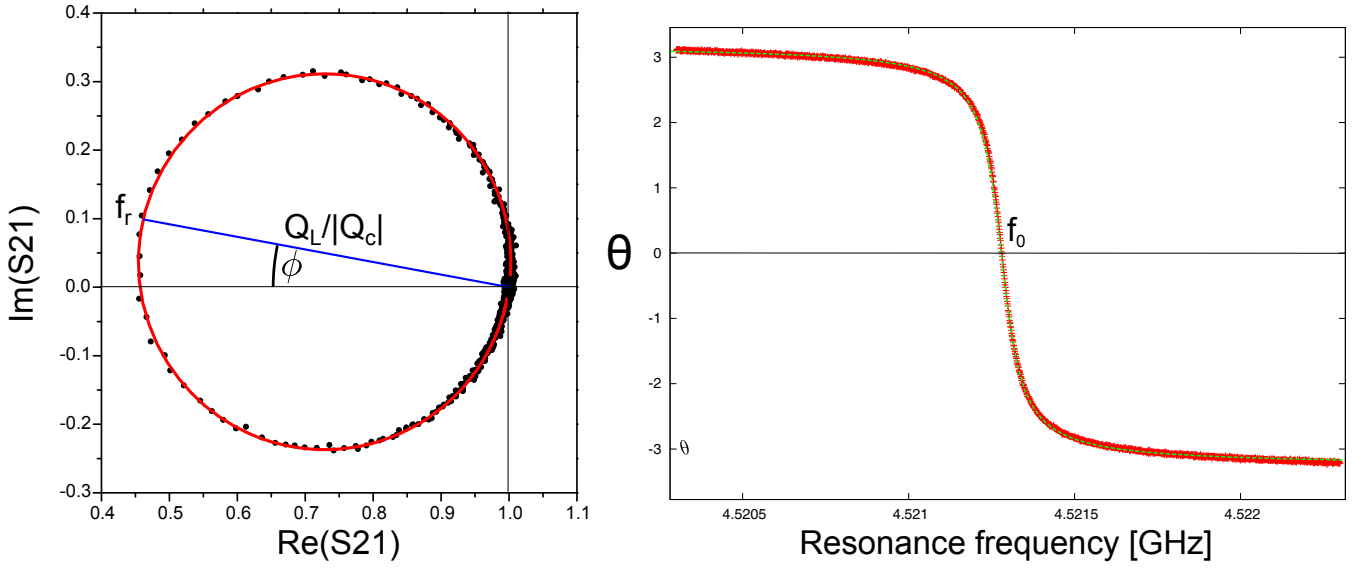
Fig. 4.4: Magnetic field sweep of the 9.5 GHz resonator. This data was taken at a temperature of 318mK and the applied power was -25dB. The arrows indicate the sweep direction.

resonance frequency and the coupling quality factor are obtained by fitting the phase. The imaginary part of S_{21} after normalisation is given by:

$$\theta = -\theta_0 + 2\arctan\left(2Q_L\left(1 - \frac{f}{f_0}\right)\right) \tag{4.2}$$

With the obtained parameters from phase and circle fit the internal quality factor can be calculated:

$$\frac{1}{Q_i} = \frac{1}{Q_L} + Re\left\{\frac{1}{|Q_c|}e^{i\Phi}\right\} \tag{4.3}$$

The error of the fit is calculated as well. The prefactors a, α and τ have to be calibrated properly before the fitting process. We are using an automated procedure to perform the fitting [44]. The circle fit is performed according to Chernov and Lesort [45].

Chapter 5

Measurement Results

When we cooled the sample down we observed a sudden decrease of 20 dB in the microwave transmission. This jump can be explained by a phase transition to the superconducting state. It occurred at a temperature of 4.3K, which is in the expected range for TiN films.

5.1 Resonator Characterisation

We observed several dips in the transmission that became narrower and deeper with decreasing temperature. The measured resonances were in the expected frequency band with the lowest resonance frequency at 3.54 GHz. The resonance frequencies did not exactly match the ones we calculated; instead they were shifted to lower values due to the kinetic inductance. The measured internal quality factors range from almost zero (dips that were even too small to fit) to 190000. A table of the measured resonator properties is provided in Appendix C.

We expected to observe seven pairs of resonances with a distance of about 1 GHz to each other. Instead, only a pair for the lowest frequency is seen, followed by single resonances at 4.5 and 5.4 GHz. In the region between 6 and 8 GHz no resonance dips can be observed. Instead there is a broad and deep dip which does not disappear at temperatures above T_c. This indicates that the resonance is not aroused by a superconducting resonator but by another device. One possibility is that this resonance is evoked by the sample box which acts as a cavity resonator. Above 9 GHz many resonance dips occur. The reason for the single dips at 4.5 and 5.4 GHz is that the resonators two and three of the chip are broken (see chapter 4.1). The broken resonators are the weakly coupled ones. For higher frequencies it is hard to assign the resonances to the resonators in the design. One reason is the broken resonators whose resonance frequencies we do not know.

A rough estimate of the kinetic inductance can be made by taking into account only the first four resonance frequencies. Their resonance frequencies amount on average 90.7% of the calculated frequencies. This leads to a kinetic inductance of 21.7% of the geometric inductance. The quality factors we measured are of more than one magnitude lower than reported values [13, 34, 30]. One reason for this may be a lack of undercut in the sample. Another reason is that the sample temperature was higher than in these works.

5.2 Temperature Dependence

We also suggest that the effective sample temperature is higher than the value determined by the temperature sensor. A reason for this might be thermal radiation from higher temperature stages and the HEMT. Before the sample there is attenuation of 30dB applied, which damps radiation by a factor 1000. Behind the sample there is only an attenuation of 6dB, which is just a factor of 4. Another heating process is microwave radiation from the surrounding copper shield. Although the chip is shielded by the sample box, stray light can still enter. This effect could be reduced by multistage shielding, as has been shown in other works [46, 47]. Another reason for a higher temperature may be a bad thermal connection to the 300 mK stage. Even if the sample itself gets cold, the arriving electrons can still have a higher effective temperature. The temperature dependence of quality factor and resonance frequency is shown in figure 5.1. When the temperature is increased the resonance frequency shifts to lower values since the kinetic inductance increases. The quality factor drops with increasing temperature. The curve does not show a saturation level at low temperatures but the gradient indicates that at temperatures below 500 mK losses due to two level systems may become important.
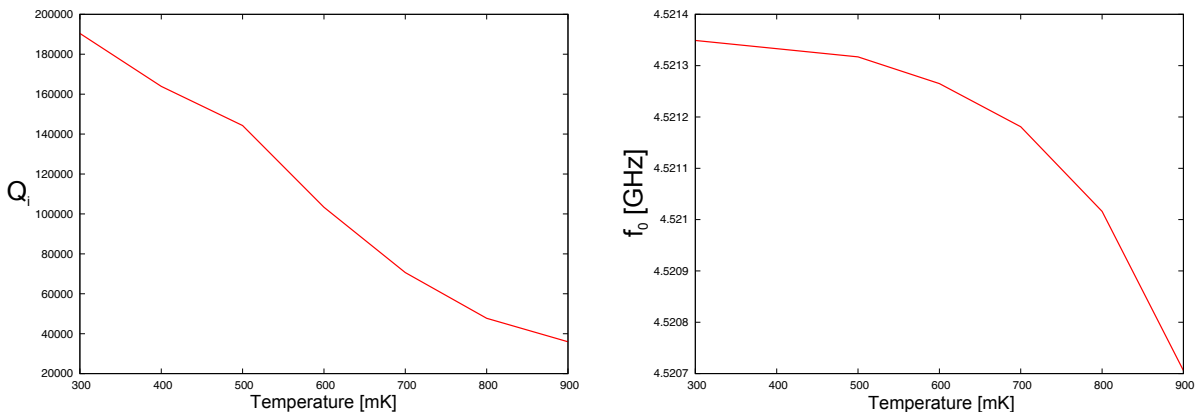

Fig. 5.1: Temperature dependence of resonance frequency and quality factor of the 4.5GHz resonator.

5.3 Power Dependence

In general, the internal quality factor decreases with decreasing power until a saturation arises [48]. A saturation indicates that the resonator is operated in the single photon regime. Figure 5.2 illustrates the power dependence of the resonator at 4.5 GHz. The quality factor is lowered with decreasing power. In the analysed interval no saturation effect can be seen, which means that we operate our resonator in the high power limit. The resonance frequency hardly exhibits any change.
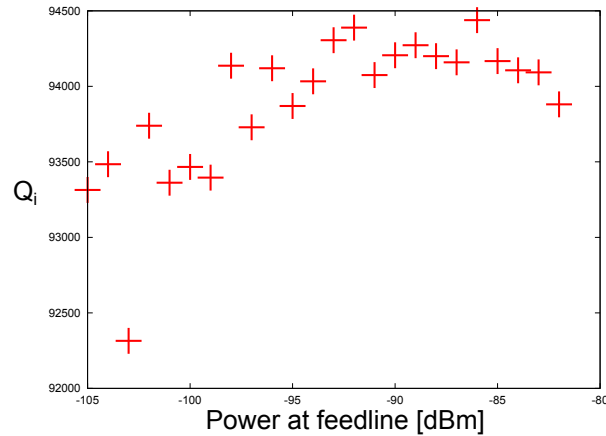
Fig. 5.2: Power dependence of quality factor of the 4.5 GHz resonator.

5.4 Magnetic Hysteresis Effects

When applying a magnetic field, we observed a change in both resonance frequency and quality factor. For the virgin sweep, the quality factor first increases with applied magnetic field in contradiction to our expectations. The reason for the rising quality factor is not the increasing magnetic field but the decreasing temperature. Although the temperature shown at the display stayed the same, the sample temperature did not. After the displayed temperature stabilised, we had to wait for almost another hour until the quality factors did not change anymore. The resonance frequency shows the expected behaviour. It decreases with rising magnetic field and when it is lowered again the frequency increases abruptly. However, its maximum value stays below the initial one.

After this first cycle, we swept the magnetic field again with the same parameters. The
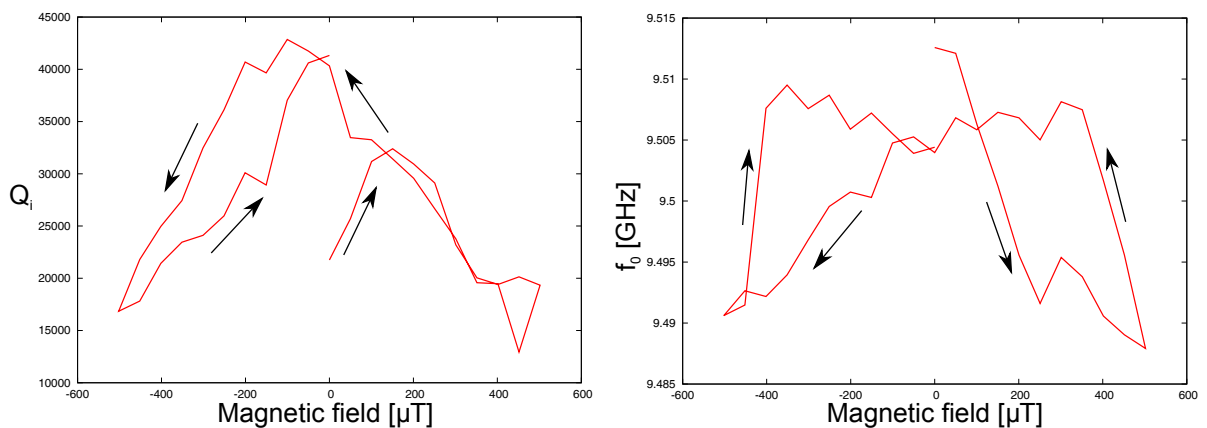

Fig. 5.3: Virgin sweep of the 9.5 GHz resonator. This data was taken at a temperature of 318mK and the applied power was -85dBm. The arrows indicate the sweep direction.

figures 5.5 and 5.4 show magnetic hysteresis loops for two resonators with different resonance frequencies, 3.5 and 9.5 GHz. The principal behaviour for both resonance frequencies is the

same. At first the resonance frequency decreases until the turning point of the magnetic field. Thereafter it rises abruptly until it almost reaches its maximum. For a magnetic field in the opposite direction the behaviour is the same, which leads to an axially symmetrical curve. Although the resonance curves show the same characteristics, they differ in the absolute change. The difference between highest and lowest frequency during one sweep is 7.6 MHz for the resonator at 3.5 GHz and 20.8 MHz for the one at 9.5 GHz. Nonetheless, the relative frequency shift is quite similar with 0.21% for the lower and 0.22% for the higher resonance frequency. This result suggests that the frequency change is caused by a modification of the kinetic inductance.

The internal quality factors also exhibit hysteresis effects, while the principal behaviour is
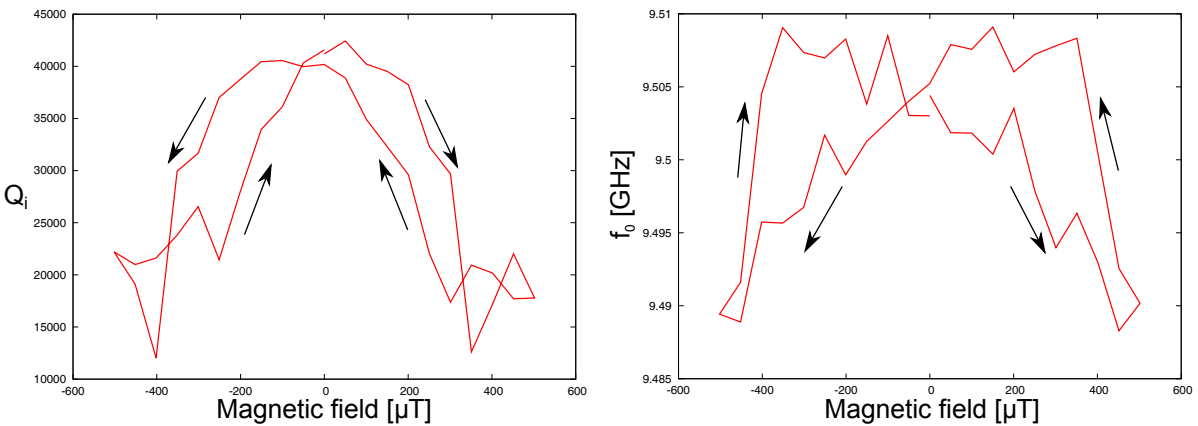
Fig. 5.4: Magnetic field sweep of the 9.5 GHz resonator. This data was taken at a temperature of 318mK and the applied power was -85dBm. The arrows indicate the sweep direction.

the same for both resonators. At first it reduces with increasing magnetic field. After a reduction of the applied magnetic field the quality factor initially stays the same. It starts to rise again when the field is reduced further. Although both values, quality factor and resonance

Fig. 5.5: Magnetic field sweep of the 3.5 GHz resonator.

Fig. 5.6: Losses of the 3.5 GHz and 9.5 GHz resonators for a magnetic field sweep.
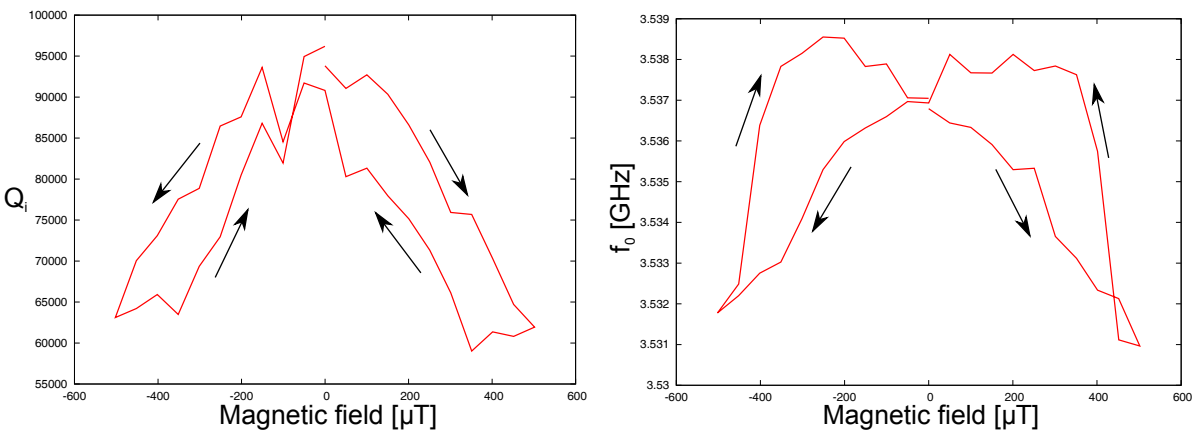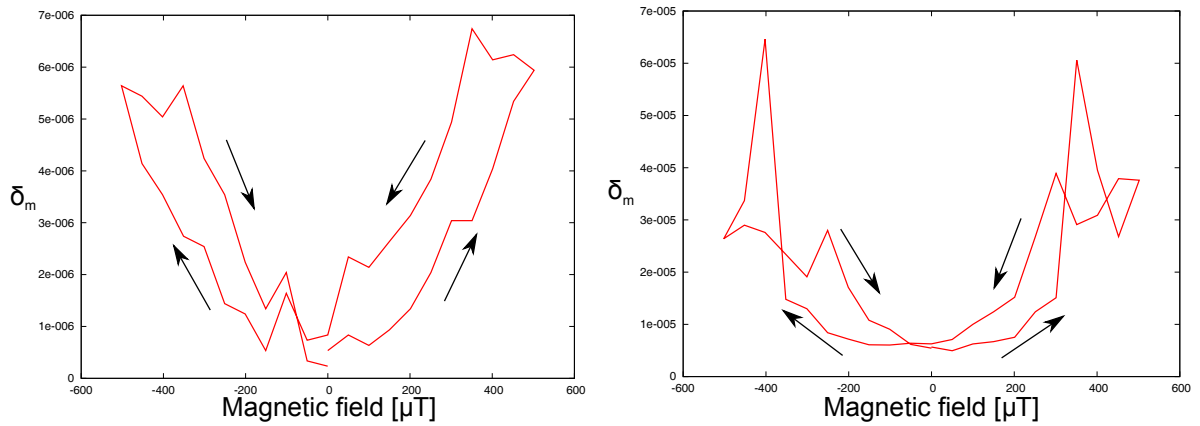
frequency show hysteresis effects, the characteristics of these curves are different. The resonance frequency increases tremendously after we decrease the absolute value of the magnetic field. In difference to that, the quality factor rises slowly. This behaviour leads to different positions of the maxima. Theory predicts a stronger initial increase for the resonance frequency as well, but the maxima are supposed to be at the same magnetic field value.

The difference between maximal and minimal quality factor is about 30000 for both resonators. If we plot the additional losses versus the magnetic field, we see a big difference between the two resonators. The additional losses for the resonator at 3.5 GHz range from $5 * 10^{-7}$ to $6 * 10^{-6}$ and for the one at 9.5 GHz from $5 * 10^{-6}$ to $6 * 10^{-5}$, which is a factor of ten. Although the difference is ssignificant, the statistical base is too weak for a conclusion on its physical origin, since we only have data for two resonators.
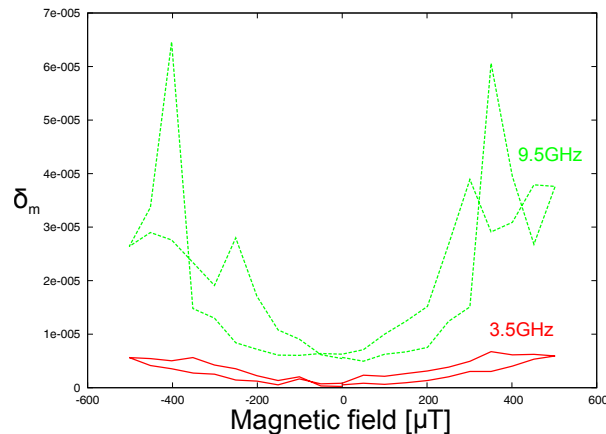

Fig. 5.7: Magnetic field sweep for the resonators at 3.5 and 9.5 GHz

All magnetic sweeps show rather saw-toothed than smooth curves. One approach to reduce this jumps is averaging over more data with a higher bandwidth. In all of the magnetic field sweeps discussed up to now we averaged 10 times with an IF bandwidth of 900. Although the
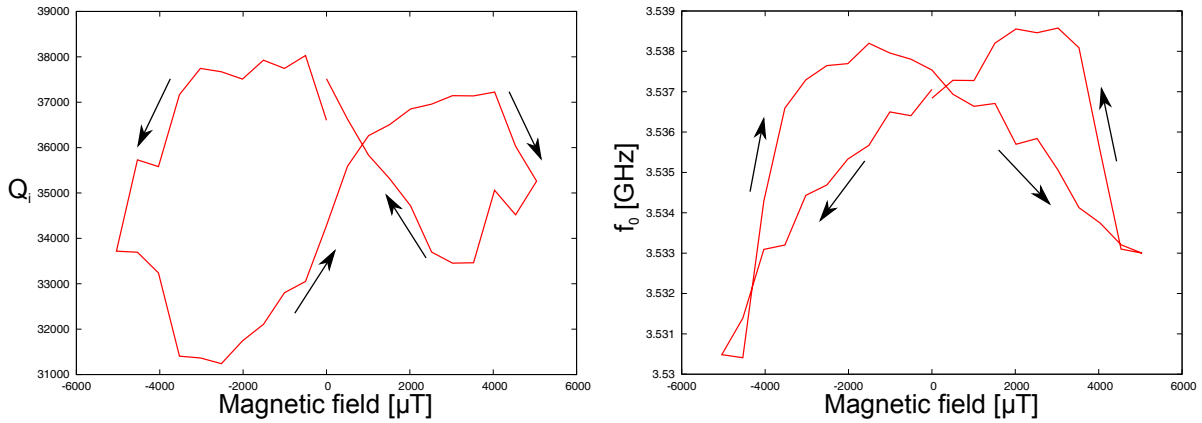
Fig. 5.8: Magnetic field sweep for the resonator at 3.5 GHz. The applied power was -85 dBm, the displayed temperature 303mK.

obtained curves look jagged the error of the circle fit remains under 0.1% for the resonator at 9.5 GHz and under 0.03% for the one at 3.5 GHz. To identify the origin of the jumps we measured the same resonator several times at a certain magnetic field. In these measurements, we could observe hardly any change in resonance frequency and only small changes in the quality factor. The current that was applied to the magnetic coil basically stayed the same. These observations suggest that the jumps in resonance frequency and quality factor are caused by differences in the vortex distribution.

After refilling helium and inserting the dipstick again, we observed smaller quality factors than in the previous measurements for all resonators, although we reached the same base temperature. We suppose that the reason for this reduced quality factors lies in worse thermal connection to the 300 mK stage or a thermal connection between a coaxial cable and the wall of the copper shield, all in all, leading to a higher effective sample temperature. Under this circumstances, it was hard to observe a hysteretic behaviour of the resonators. We had to apply higher magnetic fields in the range of 2 to 5 mT to identify reproducible magnetic hysteresis effects. The hysteresis in resonance frequency basically looks the same as for a lower sample temperature. Although the applied magnetic field is 10 times larger than in the previous measurements, the difference in frequency is 8.1 MHz; in other words, it is only 0.5 MHz larger than before. According to theory the changes should be more or less proportional to the maximal magnetic field. The higher temperature might provide a mechanism that diminishes these changes. A change in kinetic inductance can not explain this behaviour since it rises with temperature and it should lead to a higher magnetic field sensitivity. Not only does the kinetic inductance change with temperature, but the critical field H_{c1} does, too. Equation 1.1 illustrates how it reduces with increasing temperature. For a certain magnetic field value the vortex distribution depends on the critical field H_{c1}. Figure 5.9 shows the vortex distribution for a certain applied field with different values of H_{c1}. For lower critical fields more flux tubes enter the film. However, there are less vortices at the edges of the superconductor, since the
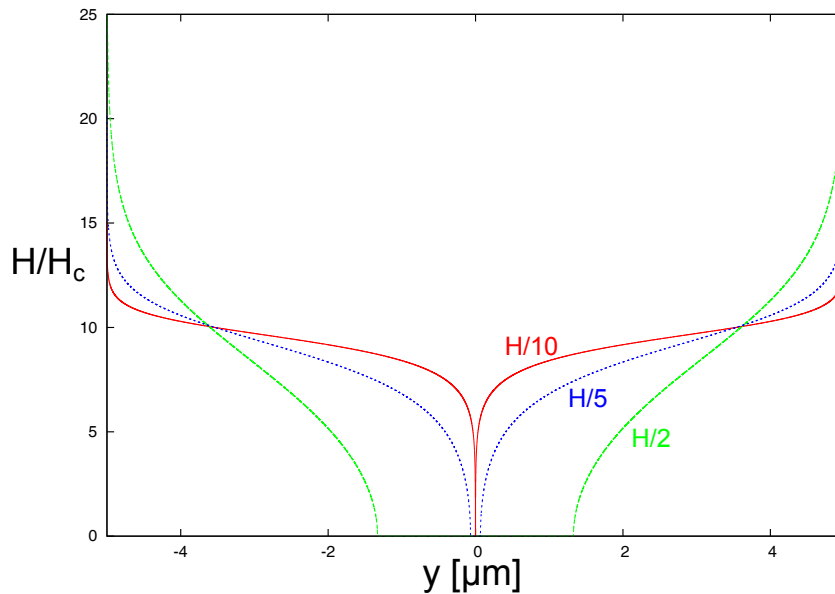
Fig. 5.9: Magnetic field distribution for different critical fields H_{c1}.

flux distribution changes, too. The changes in quality factor and resonance frequency are more sensitive to the vortices in that region, because the current is located there. As a consequence, the amplitudes of the magnetic hysteresis curves increase for lower magnetic fields.

Since the quality factors in this measurements were depressed, it was harder to observe their hysteresis effects. Figure 5.8 shows an unexpected behaviour. Instead of rising after switching the sweep direction, the quality factor decreases, which contradicts theory. As can be seen by comparing resonance frequency and quality factor, the quality factor initially stays the same and degrades at the point where the resonance frequency rises. One possible explanation is found by analysing the circle fit. It does not fit the curve well for frequencies far from resonance if there is a gradient in the baseline, which leads to a systematical error. The resonance frequency we consider here lies in a region with a strong curvature. Due to the change in resonance frequency not only do the position, but also the gradient of the baseline vary. All in all, this changes the systematical error. This effect may also occur for lower temperatures, but its impact is smaller. It might also be the reason why in the first measurements the quality factor stayed the same after changing the sweep direction. Both figures do not show axially symmetric behaviour. The points where the lines cross are shifted to the right, instead. This effect always occurred when we applied a magnetic field in one direction for a longer time than in the other direction. Another measurement was done to investigate the impact of the applied power. One sweep was done with an applied power of -85 dBm and the other one with -70 dBm, but almost no difference could be seen. One aspect we have not considered so far is that the resonators and the whole array are completely enclosed by a superconductor. Whenever a magnetic field is applied screening currents flow, that also change the magnetic field distribution in the sample and hence the hysteresis curves.
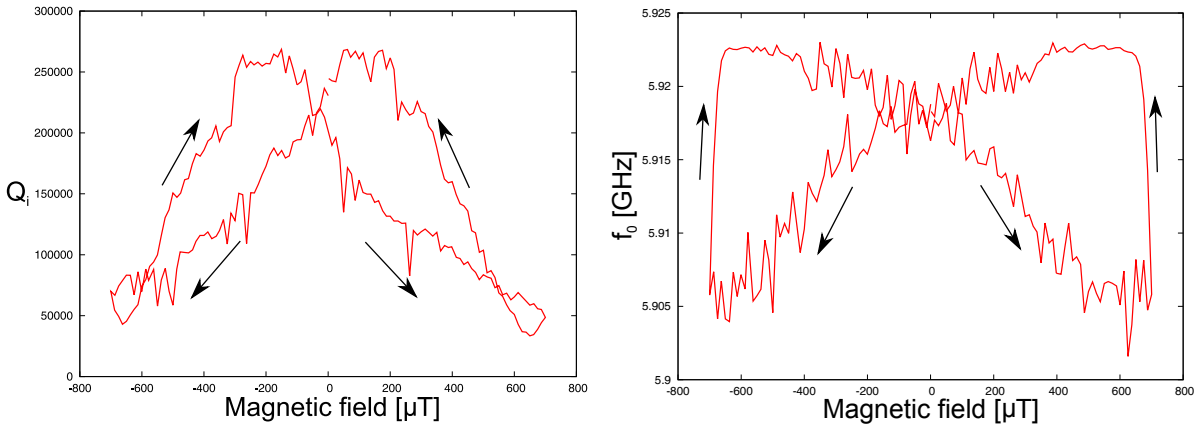
Fig. 5.10: Magnetic field sweep for a resonator at 5.9 GHz.

Another sample was measured by Fengbin Song. This sample is made of titanium nitride and consists of an array of $\frac{\lambda}{4}$-resonators. It was completely structured at NIST. In contrast to the other sample, it does not feature flux traps around the structures. Another difference is the smaller strip width and a smaller gap width in both, transmission line and resonator. The strip width is 3 and the gap width 2 μm. The measurement setup was also slightly different with only 10 dB attenuation at the lowest temperature stage. These resonators showed a similar behaviour, but with a higher sensitivity to the magnetic field. Another difference is that both, resonance frequency and quality factor, increase steeper than in the other measurements. The curve for the resonance frequency shows a very interesting behaviour. Directly after changing the sweep direction, it rises abruptly to its maximum. After this increase the resonance frequency changes very little with hardly any jumps. As the absolute value of the magnetic field is decreased further the jumps increase.

If a resonator is operated in a magnetic field, there are also ways to reduce the additional losses. For instance by sweeping the magnetic field with decreasing magnitude the vortices in the resonator can be reduced [1]. Another possibility would be to apply a higher field than the operation point first and reduce it afterwards. If the parameters are chosen properly, the magnetic field at the edges are minimised and so are the losses.

Chapter 6

Conclusion

This thesis deals with magnetic hysteresis effects in superconducting resonators, with a focus on changes in resonance frequency and quality factor. The first part of this work was to establish a procedure of structuring superconducting TiN microwave resonators at the CFN cleanroom. This was done using optical lithography and reactive ion etching. With this process we are able to produce resonators quickly and choose the parameters according to our research interest. We designed and patterned chips with arrays of several types of resonators.

These resonators showed internal quality factors of about 10^5 in the high power regime at a temperature of 300 mK. We analyse magnetic hysteresis effects in resonance frequency and quality factor of this resonators and present a theory that is able to explain these changes. Our measurements confirm the results obtained with niobium resonators [1]. The hysteresis effects we observe in resonance frequency are larger than in any reported data. We also show that these changes occur in different resonators and are proportional to the resonance frequency. A model to explain the hysteric behaviour of the resonators is given in this thesis. The resonators also differ in their magnetic field losses in a way we were not able to explain. The obtained data also indicates that these hysteresis effects depend on the sample temperature. We measured the temperature dependence of quality factor and resonance frequency as well.

In conclusion, superconducting resonators should not be operated in magnetic fields unless it is necessary. Although a tunability in resonance frequency might be desirable, it is always linked to additional losses. However, if a magnetic field is required, there are ways to reduce this losses. This can be realised by adjusting the sample parameters or changing the magnetic field history.

So far we only analysed $\frac{\lambda}{4}$-resonators. In the future we also want to analyse the lumped LC and $\frac{\lambda}{2}$-resonators that have already been fabricated. It would be interesting to investigate the magnetic behaviour of superconducting resonators further, especially the loss behaviour for different resonators. One may analyse hysteresis effects for different temperatures and in the single photon regime as well.

Bibliography

[1] D. Bothner, T. Gaber, M. Kemmler, D. Koelle, R. Kleiner, *Magnetic hysteresis effects in superconducting coplanar microwave resonators*, Phys. Rev. B **86**, 014517 (2012).

[2] P. K. Day, H. G. Leduc, B. A. Mazin, A. Vayonakis, J. Zmuidzinas, *A broadband superconducting detector suitable for use in large arrays*, Nature **425**, 817 (2003).

[3] P. Bushev, D. Bothner, J. Nagel, M. Kemmler, K. B. Konovalenko, A. Loerincz, K. Ilin, M. Siegel, D. Koelle, R. Kleiner, *Trapped electron coupled to superconducting devices*, Eur. Phys. J. D **63**, 9 (2011).

[4] A. Imamoglu, *Cavity QED Based on Collective Magnetic Dipole Coupling: Spin Ensembles as Hybrid Two-Level Systems*, Phys. Rev. Lett. **102**, 083602 (2009).

[5] P. Rabl, D. DeMille, J . M. Doyle, M. D. Lukin, R. J. Schoelkopf, P. Zoller, *Hybrid Quantum Processors: Molecular Ensembles as Quantum Memory for Solid State Circuits*, Phys. Rev. Lett. **97**, 033003 (2006).

[6] J. Verdú, H. Zoubi, Ch. Koller, J. Majer, H. Ritsch, J. Schmiedmayer, *Strong Magnetic Coupling of an Ultracold Gas to a Superconducting Waveguide Cavity*, Phys. Rev. Lett. **103**, 043603 (2009).

[7] K. Henschel, J. Majer, J. Schmiedmayer, H. Ritsch, *Cavity QED with an ultracold ensemble on a chip: Prospects for strong magnetic coupling at finite temperatures*, Phys. Rev. A **82**, 033810 (2010).

[8] C. Song, T. W. Heitmann, M. P. DeFeo, K. Yu, R. McDermott, M. Neeley, J. M. Martinis, B. L. T. Plourde, *Microwave response of vortices in superconducting thin films of Re and Al*, Phys. Rev. B **79**, 174512 (2009).

[9] J. E. Healey, T. Lindström, M. S. Colclough, C. M. Muirhead, A. Y. Tzalenchuk, *Magnetic field tuning of coplanar waveguide resonators*, Appl. Phys. Lett. **93**, 043513 (2008).

[10] C. Song, M. P. DeFeo, K. Yu, B. L. T. Plourde, *Reducing microwave loss in superconducting resonators due to trapped vortices*, Appl. Phys. Lett. **95**, 232501 (2009).

[11] D. Bothner, C. Clauss, E. Koroknay, M. Kemmler, T. Gaber, M. Jetter, M. Scheffler, P. Michler, M. Dressel, D. Koelle, R. Kleiner, *Reducing vortex losses in superconducting*

microwave resonators with microsphere patterned antidot arrays, Appl. Phys. Lett. **100**, 012601 (2012).

[12] D. Bothner, T. Gaber, M. Kemmler, D. Koelle, R. Kleiner, *Improving the performance of superconducting microwave resonators in magnetic fields*, Appl. Phys. Lett. **98**, 102504 (2011).

[13] M. Sandberg, M. R. Vissers, J. S. Kline, M. Weides, J. Gao, D. S. Wisbey, D. P. Pappas, *Etch induced microwave losses in titanium nitride superconducting resonators*, Appl. Phys. Lett. **100**, 262605 (2012).

[14] C. P. Bean, *Magnetization of hard superconductors*, Phys. Rev. Lett. **8**, 250 (1962).

[15] W. T. Norris, *Calculation of hysteresis losses in hard superconductors carrying ac: isolated inductors and edges of thin sheets*, J. Phys. D **3**, 489 (1969).

[16] E. H. Brandt, M. Indenbom, *Type-2-superconductor strip with current in a perpendicular magnetic field*, Phys. Rev. B **48**, 12893 (1993).

[17] H. Kamerlingh Onnes, *Further experiments with Liquid Helium G. On the electrical resistance of Pure Metals etc. VI. On the Sudden Change in the Rate at which the Resistance of Mercury Disappears*, Koinklijke Nederlandse Akademie van Weteschappen Proceedings Series B Physical Sciences **14**, (1911).

[18] W. Meissner, R. Ochsenfeld, *Ein neuer Effekt bei Eintritt der Supraleitfähigkeit*, Naturwissenschaften **21**, (1933).

[19] M. Tinkham, *Introduction to superconductivity* (Dover Publ., Mineola, NY, 2004).

[20] F. London, H. London, *The electromagnetic Equations of the Supraconductor*, Proc. Roy. Soc. A **149**, 71 (1935).

[21] V. L. Ginzburg, L. D. Landau, Zh. Eksp. Teor. Fiz. **20**, 1064 (1950).

[22] C. J. Gorter, H. B. J. Casimir, *Zur Thermodynamik des supraleitenden Zustandes*, Physica 1 **306**, (1934).

[23] Elektronische Eigenschaften von Festkörpern 2, Superconductivity Lecture 5, A. V. Ustinov.

[24] D. M. Pozar, *Microwave Engineering* (John Wiley and Sons, Hoboken, NJ, 2005).

[25] J. Gao, *The Physics of Superconducting Microwave Resonators*, Dissertation, California Institute of Technology, 2008.

[26] P. Drude, *Zur Ionentheorie der Metalle*, Physikalische Zeitschrift 1, 1900 **1**, 161 (1900).

[27] D. C. Mattis, J. Bardeen, *Theory of the Anomalous Skin Effect in Normal and Super-conducting Metals*, Phys. Rev. **111**, 412 (1958).

[28] R. Barends, J. J. A. Baselmans, J. N. Hovenier, J. R. Gao, S. J. C. Yates, T. M. Klapwijk, H. F. C. Hoevers, *Niobium and Tantalum High Q Resonators for Photon Detectors*, IEEE Transaction on Applied Superconductivity **17**, 263 (2007).

[29] S. Kumar, J. Gao, J. Zmuidzinas, B. A. Mazin, H. G. LeDuc, P. K. Day, *Temperature Dependence of the Frequency and Noise of Superconducting Coplanar Waveguide Resonators*, Appl. Phys. Lett. **92**, 123503 (2008).

[30] M. R. Vissers, J. S. Kline, J. Gao, D. S. Wisbey, D. P. Pappas, *Reduced microwave loss in trenched superconducting coplanar waveguides*, Appl. Phys. Lett. **100**, 082602 (2012).

[31] J. Bardeen, M. J. Stephen, *Theory of the Motion of Vortices in Superconductors*, Phys. Rev. **140**, A1197 (1965).

[32] S. K. Yip, J. A. Sauls, *Nonlinear Meissner Effect in CuO Superconductors*, Phys. Rev. Lett. **69**, 2264 (1992).

[33] Y. Krockenberger, S. Karimoto, H. Yamamoto, K. Semba, *Coherent growth of superconducting TiN thin films by plasma enhanced molecular beam epitaxy*, J. Appl. Phys. **112**, 083920 (2012).

[34] M. R. Vissers, J. Gao, D. S. Wisbey, D. A. Hite, C. C. Tsuei, A. D. Corcoles, M. Steffen, D. P. Pappas, *Low loss superconducting titanium nitride coplanar waveguide resonators*, Appl. Phys. Lett. **97**, 232509 (2010).

[35] H. G. Leduc, B. Bumble, P. K. Day, B. H. Eom, A. D. Turner, S. Golwala, D. C. Moore, O. Noroozian, J. Zmuidzinas, J. Gao, B. A. Mazin, S. McHugh, A. Merrill, *Titanium nitride films for ultrasensitive microresonator detectors*, Appl. Phys. Lett. **97**, 102509 (2010).

[36] *L-edit for physical design, Tanner EDA, data sheet (http://www.tannereda.com)*.

[37] *Sonnet Software Inc., Sonnet User's Guide, 13th edition, June 2011. (http://www.sonnetsoftware.com)*.

[38] *Nanoelectronics and information technology*, Hrsg.: R. Waser (Wiley-VCH, Weinheim, 2003).

[39] Photolithography Theory and Application of Photoresists, Etchants and Solvents; C. Koch, T. J. Rinke (2012).

[40] K. A. Blanks, A. E. Tabor, K. Becker, *Absolute cross sections for fluorine 3p->3s line emissions following single electron impact on NF3, CF4, and SF6*, J. Chem. Phys. **86**, 4871 (1987).

[41] An introduction to cryogenics, A.L. Woodcraft.

[42] M. S. Khalil, M. J. A. Stoutimore, F. C. Wellstood, K. D. Osborn, *An analysis method for asymmetric resonator transmission applied to superconducting devices*, J. Appl. Phys. **111**, 054510 (2012).

[43] A. Megrant, C. Neill, R. Barends, B. Chiaro, Y. Chen, L. Feigl, J. Kelly, E. Lucero, M. Mariantoni, P. J. J. OMalley, D. Sank, A. Vainsencher, J. Wenner, T. C. White, Y. Yin, J. Zhao, C. J. Palmstrom, J. M. Martinis, A. N. Cleland, *Planar superconducting resonators with internal quality factors above one million*, Appl. Phys. Lett. **100**, 113510 (2012).

[44] S. Probst, private communication.

[45] N. Chernov, C. Lesort, *Least Squares Fitting of Circles*, Journal of Mathematical Imaging and Vision **23**, 239 (2005).

[46] J. Baselmans, S. Yates, P. Diener, P. de Visser, *Ultra Low Background Cryogenic Test Facility for Far-Infrared Radiation Detectors*, J. Low Temp. Phys. **167**, 360 (2012).

[47] R. Barends, J. Wenner, M. Lenander, Y. Chen, R. C. Bialczak, J. Kelly, E. Lucero, P. O'Malley, M. Mariantoni, D. Sank, H. Wang, T. C. White, Y. Yin, J. Zhao, A. N. Cleland, J. M. Martinis, J. J. A. Baselmans, *Minimizing quasiparticle generation from stray infrared light in superconducting quantum circuits*, Appl. Phys. Lett. **99**, 113507 (2011).

[48] D. P. Pappas, M. R. Vissers, D. S. Wisbey, J. S. Kline, J. Gao, *Two Level System Loss in Superconducting Microwave Resonators*, EEE Trans. Appl. Supercond. **21**, 871 (2011).

Appendix A

Fabrication

Thin Film Deposition

- DC sputter deposition

- Substrate: intrinsic silicon (100)-orientation

- Remove oxide, hydrogen terminate surface with 10:1 H2O:HF solution

- Substrate temperature: 500 °C

- 1 min soak for developing thin nitride layer

- Voltage: -100 V

- Pressure: 667 mPa

- Voltage: Mixture: argon:nitrogen 3:2

- growth rate: 2nm/min

Resonator Design

- Design resonators with L-edit

- Analyse resonance frequency of single resonator with Sonnet

- Adjust resonator parameters

- Analyse again

Photomask

- Exposure with helium-cadmium-laser (420 nm)

- Develop photoresist: MF 319 for 60 s

- Etch chrome with chrome etch 18 for 60 s

Spin Coating

- Resist S1805 G2 from micro resist technology

- 500 rpm for 10 s and 4500 rpm for 90 s

- Ramp rate: 500rpm/sec

- 115 °C hotbake on Cu plate for 60 s

- 500 rpm for 10 s and 4500 rpm for 90 s

Mask Aligning

- Karl Suss MA6 mask aligner

- Power: 275 W

- Intensity: 5mW/cm^2

- Exposure time: 5 s

- Develop photoresist: MF 319 for 60 s

Reactive Ion Etching

- Sentech RIE

- Gas flow: 11 sccm SF6

- Reactor pressure: 14 Pa

- HF-Generator power: 50 W

- Etching time: 8 min

Appendix B

Chip and Sample Design

Calculated resonance frequencies for lumped LC resonators:

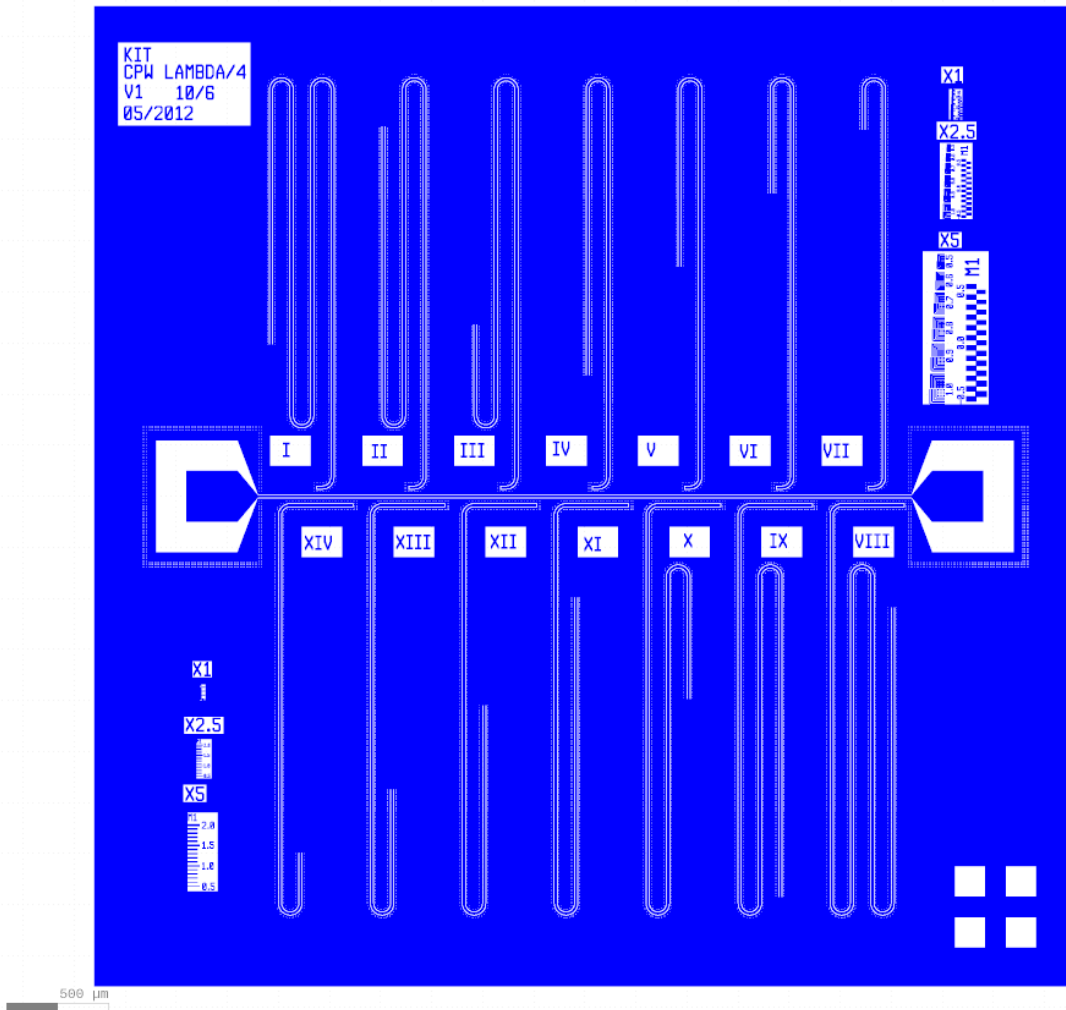| Number	Frequency [GHz]	Coupling strength
1	4.52	5k
2	4.66	100k
3	5.1	5k
4	5.21	100k
5	5.75	5k
6	5.88	100k
7	6.46	5k
8	6.6	100k
9	7.18	5k
10	7.32	100k
11	7.78	5k
12	7.94	100k
13	8.54	5k
14	8.7	100k
15	9.26	5k
16	9.36	100k
17	9.96	5k
18	10.08	100k
19	10.68	5k
20	10.78	100k
21	11.31	5k
22	11.44	100k
23	12.15	5k
24	12.25	100k

Fig. B.1: (5mm)^2 chip design with 14 $\frac{\lambda}{4}$-resonators. The strip width of the resonators is 10 μm and the gap width 6 μm. The blue regions shall be superconductor, the small dots around the structures are flux traps.

Calculated frequencies for the narrow $\frac{\lambda}{4}$-resonators:

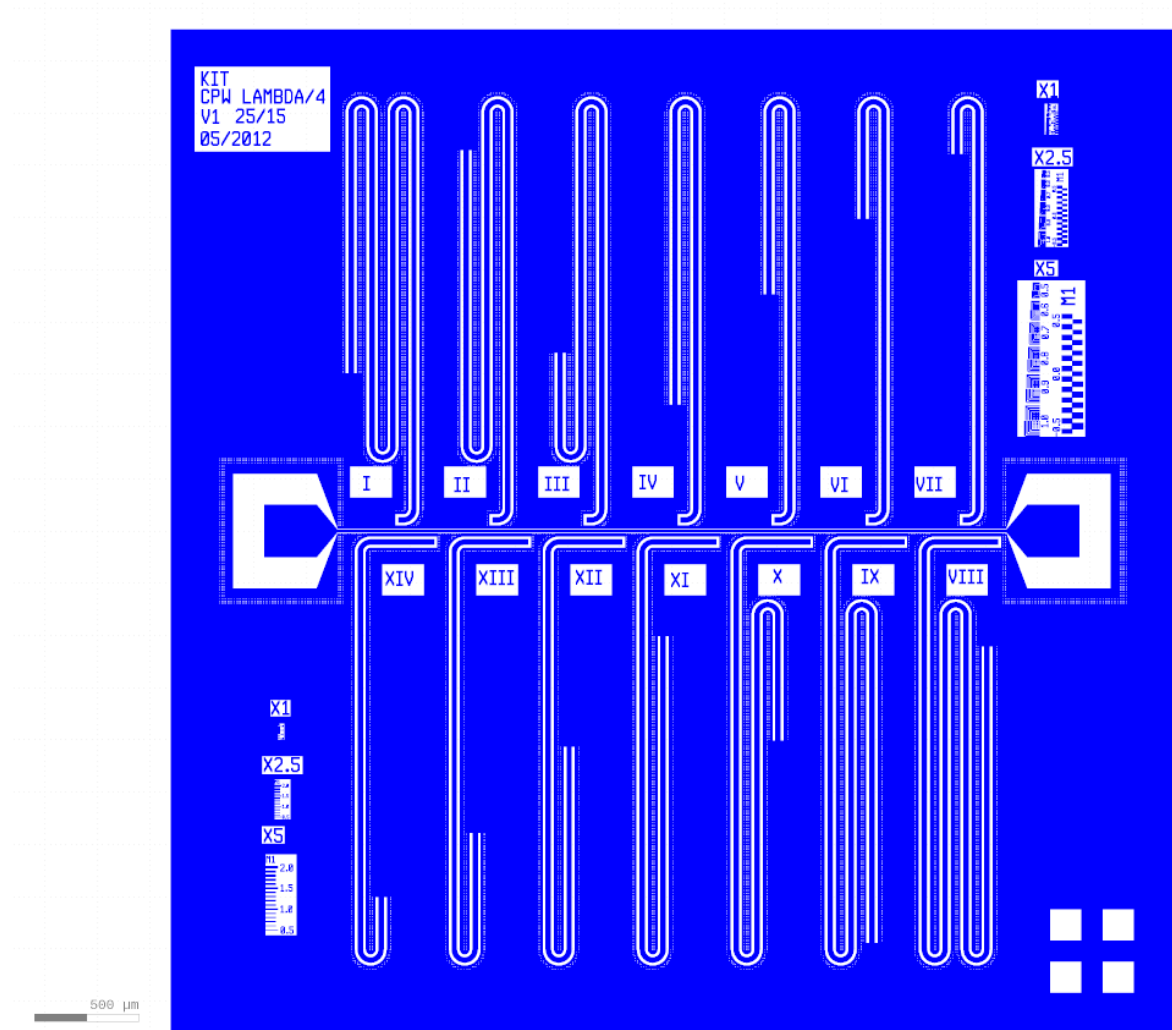| Number	Frequency [GHz]	length [mm]
I, XIII	4	7.35
II, IX	5	5.88
III, X	6	4.9
IV, XI	7	4.2
V, XII	8	3.68
VI, XIII	9	3.27
VII, XIV	10	2.94

Fig. B.2: $(5mm)^2$ chip design with 14 $\frac{\lambda}{4}$-resonators. The strip width of the resonators is 25 μm and the gap width 15 μm. The blue regions shall be superconductor, the small dots around the structures are flux traps.

Calculated frequencies for the broad $\frac{\lambda}{4}$-resonators:

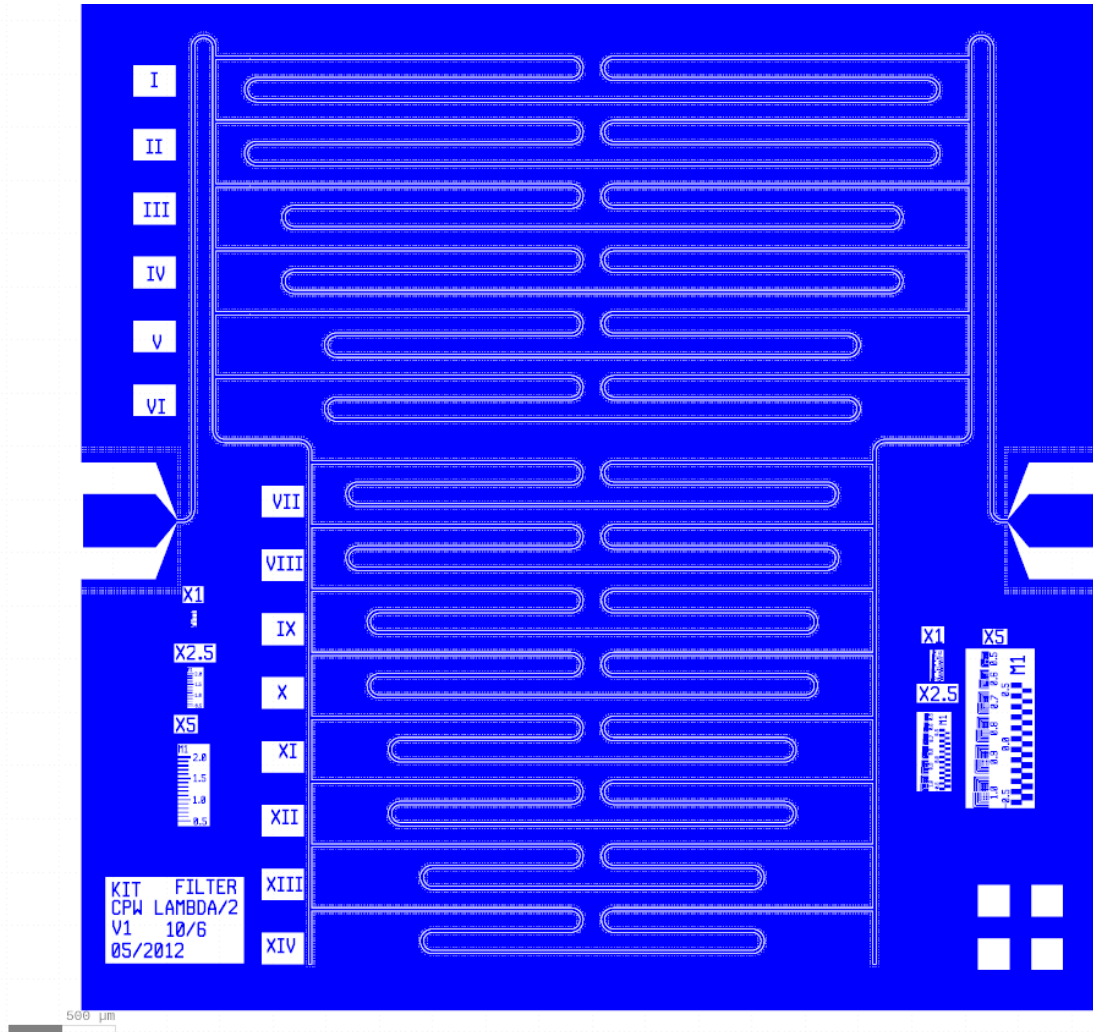| Number	Frequency [GHz]	length [mm]
I, XIII	4	7.35
II, IX	5	5.88
III, X	6	4.9
IV, XI	7	4.2
V, XII	8	3.68
VI, XIII	9	3.27
VII, XIV	10	2.94

Fig. B.3: $(5\text{mm})^2$ chip design with 14 $\frac{\lambda}{2}$-resonators. The blue regions shall be superconductor, the small dots around the structures are flux traps.

Calculated frequencies for the $\frac{\lambda}{2}$-resonators:

Number	Frequency [GHz]	length [mm]
I, II	6	4.81
III, IV	7	4.26
V, VI	7.5	3.86
VII, VIII	8	3.61
IX, X	8.5	3.41
XI, XII	9	3.21
XIII, XIV	10	2.91

Appendix C

Measurements

Frequency [GHz]	Loaded Q	Internal Q	Coupling Q
3.541	7621	98377	8986
3.749	-	-	-
4.521	55154	118740	102993
5.409	26533	94397	63906
8.323	255	423	645
8.534	-	-	-
8.646	2976	3722	14849
9.515	7605	53707	8859
9.639	26452	55382	52723
10.489	9178	46254	11450
10.505	1749	5573	2549
10.899	47375	71129	141859
11.219	29434	53238	65799

The hyphens mean that we did see a resonance, but the dip was too small to measure.
The resonator at 10.489 GHz or the one at 10.505 GHz may be the second harmonic of the resonator with the lowest resonance frequency.

Acknowledgments

First of all I thank Professor Alexey V. Ustinov for giving me the opportunity to do my diploma thesis in his group.

I also thank Professor Weißwho agreed to be the second reviewer of this thesis.

Of course I am grateful to my supervisor Dr. Martin Weides, from whom I could learn a lot.

I also want to thank the whole fluxon group for providing a pleasant working atmosphere.

Special thanks go to Fengbin Song who not only helped me with the measurement setup but also gave me an insight in the chinese culture.

I want to thank Dr. Hannes Rotzinger, too, who always took the time to answer my questions.

I am grateful to Sebastian Probst as well, who helped me in stressfull times.

Another thank-you goes to Kirill Lakhmansky who introduced me to the unknown world of the cleanroom.

I would like to thank Mr. Penzel, too, who had at least as much trouble with the helium can as I did.

I also thank the guys from room 4.10 (including Grigorij) for a lot of laughter and interesting discussions.

Of course I thank my friends as well who made me enjoy the whole studies and were there for me when I needed them.

Especially I thank Lukas Ofer who guided me through the jungle of the english language.

Last but not least I thank my family, who always supported me.

Kennst du die Welt, wo die Photonen glühn?
Du kennst sie nicht?-Du sollst sie kennenlernen.
Wo Quarks in allerschönsten Farben blühn
und sich vermehren, wenn sie sich entfernen.

Wo eine Katze zeitgleich lebt und stirbt;
dort lässt sich noch das Unteilbare teilen.
In einer Welt, wo Gott die Würfel wirft,
da kann man hier und dort zugleich verweilen.

Die Professoren dort sind schön und kühn
und wissen alles, vom Atom bis zu den Sternen.
Kennst du die Welt, wo die Photonen glühn?
Du kennst sie nicht?-Du musst sie kennenlernen.

Erklärung

Hiermit erkläre ich, diese Arbeit selbstständig und unter ausschließlicher Verwendung der angegebenen Literatur angefertigt zu haben.

_____   _____
(Ort, Datum)   (Philipp Mayer)